

## MENTATION PAGE

Form Approved  
OMB No 0704-0188

AD-A281 788



In my capacity as a burden estimator, I am responsible for reviewing instructions, searching existing data sources, and estimating the time required to document and analyze the collection of information. Send comments regarding this burden estimate or any other aspect of this reporting burden to Washington Headquarters Services, Directorate for Information Operations and Reports, DIA/DS/DRBMS, 3700 F Street, NW, Washington, DC 20330.

REPORT DATE

3. REPORT TYPE AND DATES COVERED

THESES/DISSERTATION

4. TITLE AND SUBTITLE

An Application of Singularity Analysis To A Heavy Precipitation Event

5. FUNDING NUMBERS

6. AUTHOR(S)

Barbara Lee Cieslik

7. PERFORMING ORGANIZATION NAME(S) AND ADDRESS(ES)

AFIT Student Attending:

Univ. of Oklahoma

8. PERFORMING ORGANIZATION REPORT NUMBER

AFIT/CI/CIA-  
94-031

9. SPONSORING/MONITORING AGENCY NAME(S) AND ADDRESS(ES)

DEPARTMENT OF THE AIR FORCE  
AFIT/CI  
2950 P STREET  
WRIGHT-PATTERSON AFB OH 45433-7765

10. SPONSORING/MONITORING AGENCY REPORT NUMBER

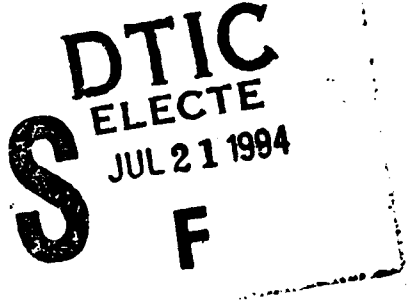
11. SUPPLEMENTARY NOTES

12a. DISTRIBUTION/AVAILABILITY STATEMENT

Approved for Public Release IAW 190-1  
Distribution Unlimited  
MICHAEL M. BRICKER, SMSgt, USAF  
Chief Administration

12b. DISTRIBUTION CODE

13. ABSTRACT (Maximum 200 words)



11308 94-22687

DTIC QUALITY INSPECTED 8

94 7 19 161

14. SUBJECT TERMS

15. NUMBER OF PAGES

100

16. PRICE CODE

17. SECURITY CLASSIFICATION OF REPORT

18. SECURITY CLASSIFICATION OF THIS PAGE

19. SECURITY CLASSIFICATION OF ABSTRACT

20. LIMITATION OF ABSTRACT

94-031

THE UNIVERSITY OF OKLAHOMA  
GRADUATE COLLEGE

AN APPLICATION OF SINGULARITY ANALYSIS  
TO A HEAVY PRECIPITATION EVENT

A THESIS  
SUBMITTED TO THE GRADUATE FACULTY  
in partial fulfillment of the requirements for the  
degree of  
MASTER OF SCIENCE IN METEOROLOGY

Accesion For	
NTIS CRA&I	<input checked="" type="checkbox"/>
DTIC TAB	<input type="checkbox"/>
Unannounced	<input type="checkbox"/>
Justification _____	
By _____	
Distribution / _____	
Availability Codes	
Dist	Avail and/or Special
A-1	

By  
BARBARA LEE CIESLIK  
Norman, Oklahoma  
1993

AN APPLICATION OF SINGULARITY ANALYSIS

TO A HEAVY PRECIPITATION EVENT

A THESIS

APPROVED FOR THE SCHOOL OF METEOROLOGY

BY

Mark K. Sane

Frederick H. Carr

Edward A. Brandes

**DEPARTMENT OF THE AIR FORCE  
8th Operations Support Squadron (PACAF)  
APO AP 96264-2139**

**17 Feb 94**

**MEMORANDUM FOR AFIT/CIR**

**ATTN: Major M. Smith  
Wright -Patterson AFB, OH 45433-6583**

**FROM: Capt Barbara Cieslik  
8 OSS/OSW  
PSC #2, Box 3086  
APO AP 96264-3086**

**SUBJECT: Final AFIT Education Plan and Thesis Transmittal Letter**

1. Attached, you will find my final Education Plan and a copy of my Masters' thesis submitted to the faculty of the University of Oklahoma. I apologize for the tardiness of this package, but I had some problems confirming that the degree had actually been conferred and our local exercise schedule has been very full. You should have already received a copy of my transcript with the degree posted. However, I will have another copy sent to you in the next few weeks.
2. Please note that any fees or tuition associated with the courses taken after July 1990 were paid for by me. No fees were assessed against the Air Force or AFIT after that date.
3. Please call me (DSN 782-4501) if you require any other information in order to post my degree to my Air Force records.



**BARBARA L. CIESLIK, Captain, USAF  
Commander, Weather Flight**

**Attachments:**

1. AFIT Final Education Plan
2. Masters' Thesis (unbound)

**c Copyright by Barbara Lee Cieslik 1993  
All Rights Reserved**

## **ACKNOWLEDGEMENTS**

I wish to thank the members of my committee, Dr Yoshi Sasaki, Dr Fred Carr and Dr Ed Brandes for their thought-provoking questions and guidance throughout this investigation. I also wish to thank Dr Sasaki for his steadfast support and understanding.

Dan Frashier and Bryan Tilley were particularly helpful in helping me understand the radar data and how to manipulate it. Their insight was greatly appreciated. Exchanging ideas and thoughts with them usually lead to new discoveries. Dan provided the 4/3 earth plot of height vs. range in Chapter IV.

Thank you to the many graduate students in the department who helped me with various little projects: Mark Shafer, Steve Lazarus, Meta Sienkiewicz, Tim Hughes and others. Thank you to my "partner in crime" Mark Mesenbrink for allowing me to abuse his computer.

Thank you to the National Severe Storms Laboratory for providing the radar data. I would like to thank Bill Chapman of the University of Illinois at Champaign-Urbana who provided me with synoptic data for this investigation. Thanks to Mark Shafer for arranging this little "data transfer."

My heartfelt thanks goes to the members of the 45th Weather Squadron and the DoD Manager's Space Shuttle Contingency Support

Office who cheered me through the last few days of my work.

Finally, I would like to thank the United States Air Force for giving me this opportunity to obtain a Master's degree.

This investigation was supported by National Aeronautics and Space Administration (NASA) grant NAG9-228 and National Science Foundation (NSF) grant ATM-8417654.

## TABLE OF CONTENTS

	Page
LIST OF ILLUSTRATIONS .....	vii
Chapter	
I. INTRODUCTION .....	1
II. SYNOPTIC OVERVIEW .....	5
III. ANALYTICAL METHODS .....	19
3.1 Singularity Extraction .....	19
3.2 Precipitation Analysis .....	29
IV. RESULTS AND DISCUSSION .....	32
4.1 Meteorological Features .....	34
4.2 Background Features .....	48
4.3 Folded Features .....	63
V. CONCLUSIONS .....	71
VI. FUTURE WORK .....	74
BIBLIOGRAPHY .....	76
APPENDIX A .....	82
APPENDIX B .....	91

## **LIST OF ILLUSTRATIONS**

<b>Figure</b>		<b>Page</b>
2.1.a	0300 GMT 27 May 1987 Surface Analysis .....	6
2.1.b	Geostationary Operational Environmental Satellite (GOES) Enhanced Infra-Red (EIR) Sector Picture from 0301 GMT 27 May 1987 .....	6
2.2.a	1200 GMT 27 May 1987 Surface Analysis .....	7
2.2.b	1201 GMT 27 May 1987 GOES EIR .....	7
2.3	2001 GMT 27 May 1987 GOES EIR .....	9
2.4	GOES EIR MB Enhancement Curve .....	10
2.5.a	0000 GMT 28 May 1987 Surface Analysis .....	14
2.5.b	GOES EIR 0031 GMT 28 May 1987 .....	14
2.6	0000 GMT 28 May 1987 Skew-T .....	15
2.7	0000 GMT 28 May 1987 850 mb Analysis .....	16
2.8.a	0000 GMT 28 May 1987 700 mb Analysis .....	17
2.8.b	0000 GMT 28 May 1987 500 mb Analysis .....	17
2.9	0000 GMT 28 May 1987 250 mb Analysis .....	18
3.1	Local Symmetry Singularity .....	21
3.2	Rankine Combined Velocity Profile .....	23
3.3	Singularity Computation Steps .....	26
3.4	Raingage Locations and Analysis Grid .....	31
4.1	Volume Scan Heights .....	33
4.2.a	233256 GMT 27 May 1987 Singularity Analysis ..	35

4.2.b	233256 GMT 27 May 1987 Reflectivity .....	36
4.2.c	233256 GMT 27 May 1987 Velocity .....	37
4.3	234239 GMT 27 May 1987 Singularity Analysis ..	39
4.4	235221 GMT 27 May 1987 Singularity Analysis ..	40
4.5	000205 GMT 28 May 1987 Singularity Analysis ..	41
4.6	001148 GMT 28 May 1987 Singularity Analysis ..	42
4.7	232618 GMT 27 May 1987 Singularity Analysis ..	44
4.8	233601 GMT 27 May 1987 Singularity Analysis ..	45
4.9	234543 GMT 27 May 1987 Singularity Analysis ..	46
4.10	235526 GMT 27 May 1987 Singularity Analysis ..	47
4.11	234239 GMT 27 May 1987 Singularity Analysis ..	49
4.12	Model of a Squall Line .....	50
4.13	233256 GMT 27 May 1987 Singularity Analysis ..	51
4.14	235221 GMT 27 May 1987 Singularity Analysis ..	52
4.15	000205 GMT 28 May 1987 Singularity Analysis ..	53
4.16	Time-Series of Low-Level Average Background Divergence .....	55
4.17	231636 GMT 27 May 1987 Singularity Analysis ..	56
4.18	232618 GMT 27 May 1987 Singularity Analysis ..	57
4.19	233601 GMT 27 May 1987 Singularity Analysis ..	58
4.20	234543 GMT 27 May 1987 Singularity Analysis ..	59
4.21	Time-Series of Mid-Level Average Background Divergence .....	60
4.22	005342 GMT 28 May 1987 Singularity Analysis ..	61
4.23	Cross-Section of a Thunderstorm Showing New Development Along the Gust Front .....	62
4.24	234746 GMT 27 May 1987 Singularity Analysis ..	64

4.25	Time-Series of Low-Level Average Background Divergence and the Occurrence of Aliasing ....	66
4.26	Schematic of the Aliasing with Respect to the Singularities .....	67
B.1	The Relationship Between Grid Size and Data Spacing .....	97

## **ABSTRACT**

On 27 May 1987, a mesoscale convective complex (MCC) brought heavy rains and flash flooding to the central portion of Oklahoma. A two-pass Barnes analysis is used to analyze the rainfall data recorded by 29 raingage instruments in the Oklahoma raingage network. The precipitation analysis is compared with a singularity analysis of Doppler velocity data. The singularity analysis produced three separable classes of divergence singularities:

1. divergence singularities associated with a gust front,
2. divergence singularities associated with the precipitation, and
3. divergence singularities associated with velocity folding.

These three classes are shown to be separable based on the order of magnitude and singularity configurations. This relatively simple and quick analysis method can help

reduce the number of data points a radar operator needs to absorb. It can also provide a lead-time of 30 minutes or more for meteorologically significant events such as gust fronts and a lead-time of approximately 10 minutes for heavy precipitation.

**AN APPLICATION OF SINGULARITY ANALYSIS  
TO A HEAVY PRECIPITATION EVENT**

**CHAPTER I**

**INTRODUCTION**

Over the years since the Doppler radar was first developed, meteorologists have sought to extract as much information as possible from the velocity and reflectivity data. Based on current estimates of the spacing between radars in the Next Generation Weather Radar (NEXRAD) Doppler radar network, extraction of information will essentially be from a single radar during convective activity. Since we desire to know as much as possible about the wind vector field, we need to maximize the amount of information the single wind component provides.

In 1969, Peace, et al., hypothesized that as an echo moves across a radar's field of view, there is very little change in the wind field structure. This means that the wind field can be considered essentially unchanged when viewed by a radar at two different times. The basic premise is that the wind field is linear in time. The Velocity Azimuth Display (VAD) developed by Lhermitte and Atlas (1961) utilizes the linear character of the wind field to produce the

mean horizontal wind field. The primary disadvantage of this technique is that it requires the radar to be surrounded by scatterers. Other investigators (Caton, 1963; Browning and Wexler, 1968) have extended the VAD to yield other important parameters: mean convergence and stretching and shearing deformations. Here, the basic assumption introduced and used is that the wind field varies in a linear fashion in the horizontal. In 1975, Easterbrook showed that five parameters of the wind field can be extracted when a conical, rather than circular, surface is used. He found that the mean horizontal velocity determined in this way is contaminated by vorticity, and, thus, would require additional information to accurately determine it. In 1979, Waldteufel and Corbin extended the linear assumption of the wind field during two different observations at the same elevation angle to include the volume traced out by the radar. They determined that analyzing a volume provides information on mesoscale features.

The Doppler radar uses phase shifts in the returned radiation to determine the velocity of a target (Battan, 1973). The pulse repetition frequency (PRF) uniquely determines the maximum Doppler shift frequency, which, in turn, uniquely determines the maximum velocity (unambiguous velocity) that can be detected by the radar. If a measured velocity is greater than the unambiguous velocity, it is aliased, or folded (Atlas, 1964). A reliable objective method of unfolding these velocities in real-time is still in development.

Currently, there are several types of velocity analyses in use. They differ in how the averaged velocity samples are used and how

they are calculated. The gust front algorithm used in the Terminal Doppler Weather Radar (TDWR) uses a running average that looks for decreasing average velocities over a prescribed distance of 2-5 km to produce pattern vectors (Witt, et al., 1989). The pattern vectors then use a vertical continuity constraint to help the algorithm produce a 10 and 20 minute forecast of the gust front position and the wind speed and direction behind it. A group at the National Severe Storms Laboratory (NSSL) is working on an improvement to this algorithm that also incorporates a thin line estimate from the reflectivity data, as well as what is termed the azimuthal shear (velocity segments from oblique angles to the gust front, vice perpendicular, along the radial) (Eilts, et al., 1991). The National Center for Atmospheric Research (NCAR) uses a radial velocity scheme with their CP-4 Doppler radar that averages two sets of three data gates separated by approximately 2 km. The two averaged velocities are then subtracted and divided by the distance between (Kessinger, 1991).

This investigation began as an effort to determine a relatively simple technique for finding a correlation between the flow characteristics extracted from the Doppler wind field and localized, heavy precipitation. The limited case chosen was the occurrence of a mesoscale convective complex (MCC) that caused significant flash flooding throughout the state of Oklahoma on 27 May 1987 (NOAA, 1987b).

The technique investigated focused on three distinct features extracted from the singularity analysis first suggested by Sasaki, et

al. (1988). They are gust front, background divergence and velocity folding. These three features are separable quantitatively and qualitatively. The storm features are shown to indicate the presence of a gust front (or outflow boundary) above the boundary layer almost 30 minutes before the Doppler wind field indicated a gust front signature at low-levels. The storm features also show indications of the gust front at low-levels 20 minutes prior to the appearance of the signature.

The background features (divergence values less than  $8 \times 10^{-3} \text{ ms}^{-1}$ ) proved to be a good indicator of where the heaviest precipitation and the downdraft were located. It also proved to be a good indicator of when the upper-levels (elevations greater than  $4^\circ$ ) would have aliased winds. Differences in low- and mid-level background values proved to be helpful in determining the onset of heavy precipitation. The mid-level background values were used to determine where the heavy precipitation was located.

The folded features (divergence values greater than  $2 \times 10^{-2} \text{ ms}^{-1}$ ) showed patterns that can uniquely identify the location of aliasing and also the wind direction at higher elevation angles.

## **CHAPTER II**

### **SYNOPTIC OVERVIEW**

In this chapter, we review the development of the storm of 27-28 May 1987. We also determine the nature of the storm and review its expected characteristics.

At 0300 GMT on 27 May 1987, the surface chart (Fig. 2.1.a) shows a large frontal system extending from a low of 1001 millibars (mb) in western South Dakota eastward through the Great Lakes and into western New York state. A cold front reaches southward into the Big Bend region of Texas. A trough extends from the vicinity of Amarillo, Texas, through western Oklahoma and into southwestern Wisconsin. The satellite picture (Fig. 2.1.b) shows cold cloud top temperatures associated with thunderstorm activity along the trough. The trough axis and the cold front to its west are of interest throughout the remaining discussion.

Nine hours later, the thunderstorm activity through

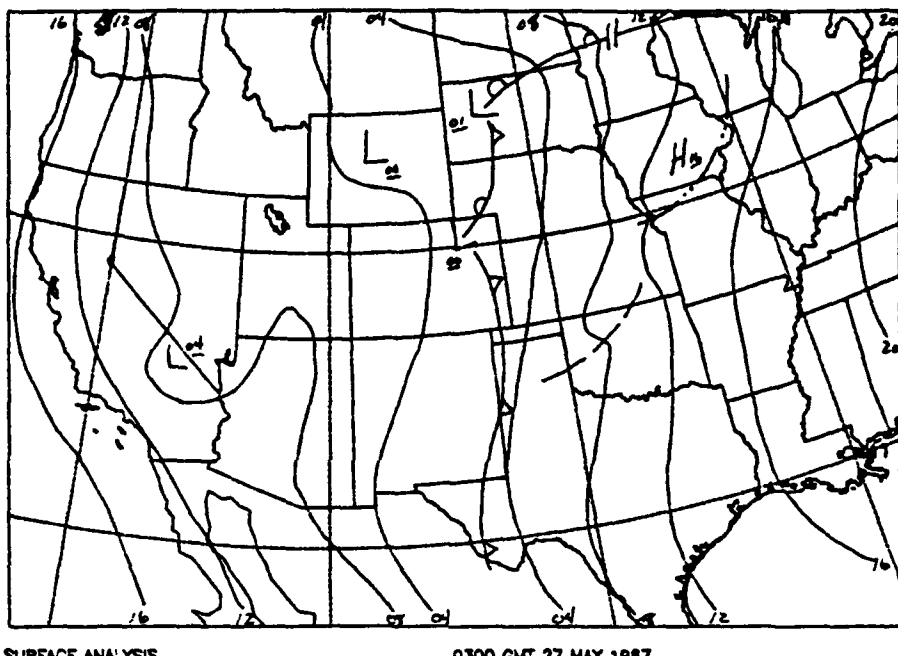


Fig. 2.1.a 0300 GMT 27 May 1987 surface analysis

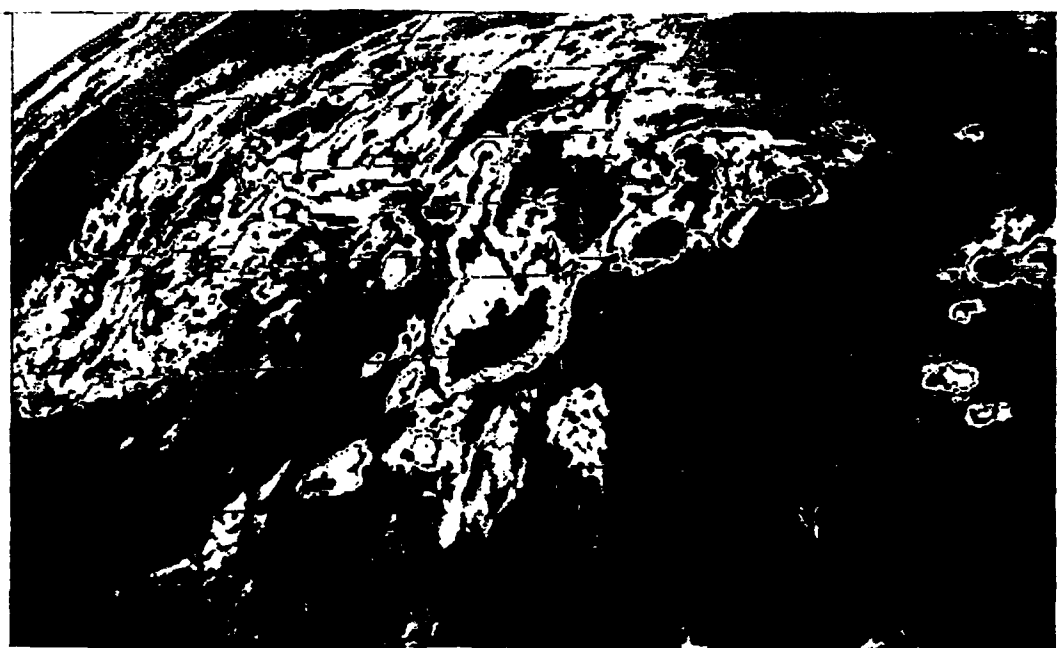
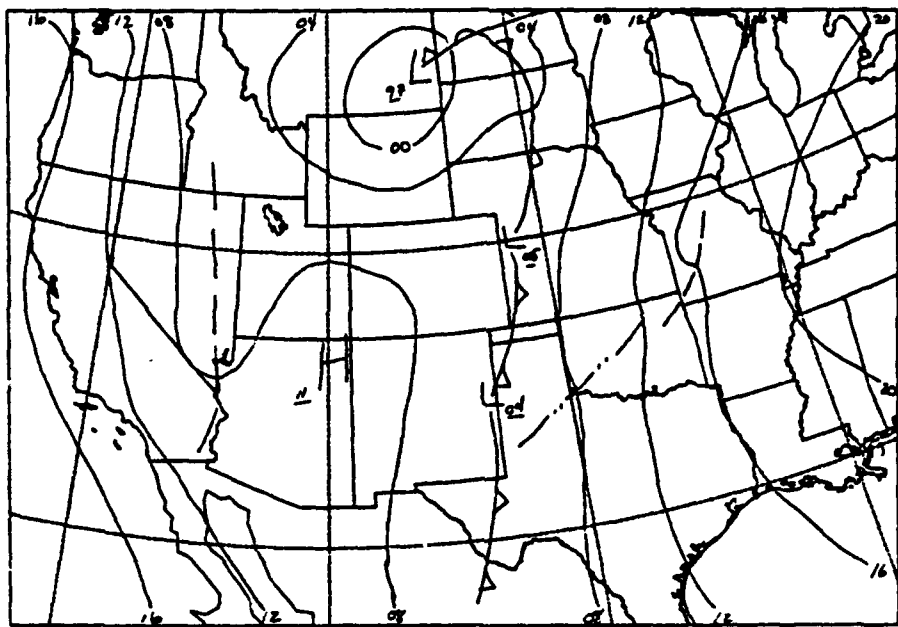


Fig. 2.1.b Geostationary Operational Environmental Satellite (GOES) enhanced infra-red (EIR) sector picture from 0301 GMT (2101 CST) 27 May 1987



SURFACE ANALYSIS

1200 GMT 27 MAY 1987

Fig. 2.2.b 1200 GMT 27 May 1987 surface analysis

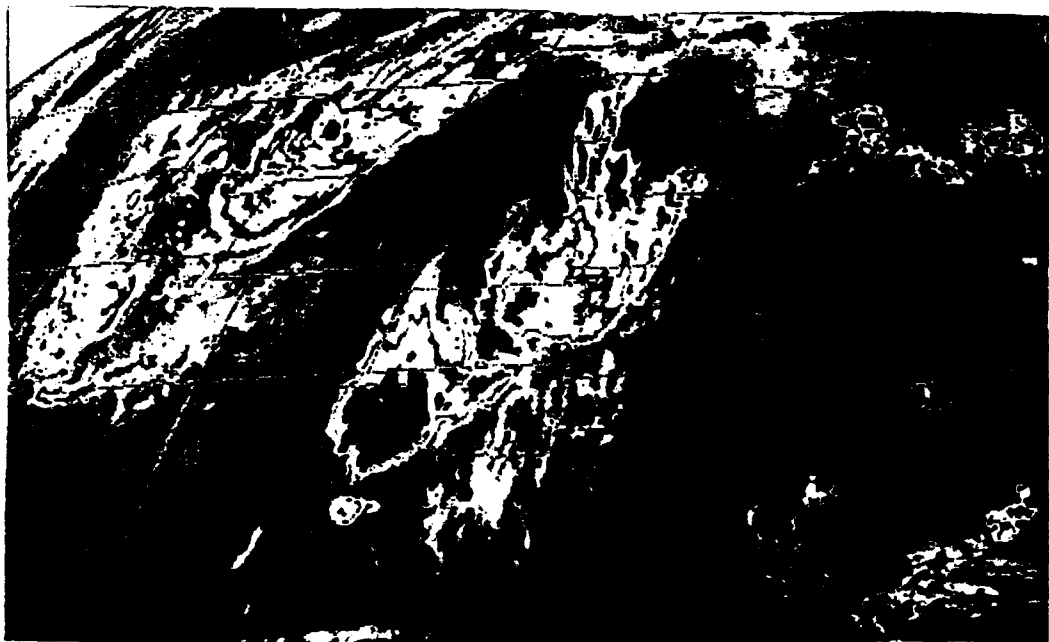


Fig. 2.2.b 1201 GMT 27 May 1987 GOES EIP sector picture

the Texas panhandle and western Oklahoma has increased (Fig. 2.2.b). The stations just to the north of the squall line on the surface chart (Fig. 2.2.a) indicate thunderstorms, and a little farther north, the stations indicate rainshowers. Note that the front in western Texas has not moved over the past nine hours. This will be identified as a dry line later in the day by the National Meteorological Center (NMC).

By 2000 GMT the activity has moved into central Oklahoma and has a fairly extensive cirrus shield (Fig. 2.3). Up to this point, the NMC charts have identified the feature over Oklahoma as a squall line, but is this really the case? Leary and Rappaport (1987) determined that a mesoscale convective complex (MCC) and a squall line have very similar echo structures and low-level dynamic and thermodynamic characteristics. This is because they are both subsets of a much larger class of storms known as mesoscale convective systems (MCS; Knupp and Cotton, 1987). Their primary differences are in the areal extent and longevity (Maddox, 1980, 1983). The MCC is one of the most important weather systems in the Great Plains, because it accounts for most of the precipitation and severe weather during the summer (Maddox, et al., 1982; Rodgers, et al., 1983, 1984; Fritsch, et al., 1986; Augustine and Howard, 1988).

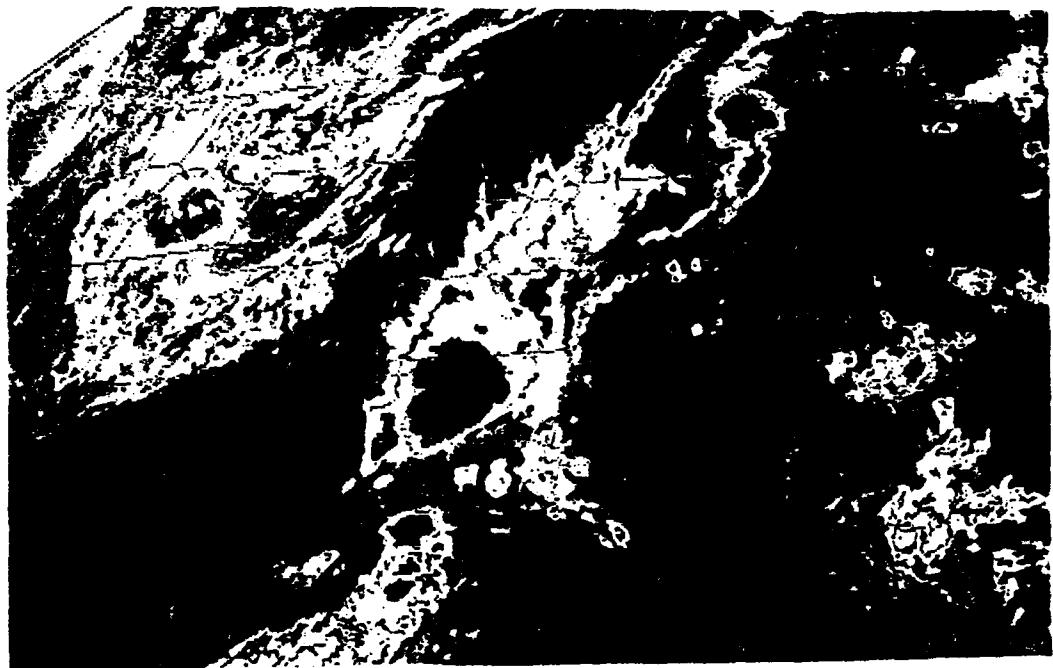


Fig. 2.3 2001 GMT 27 May 1987 GOES EIR sector picture

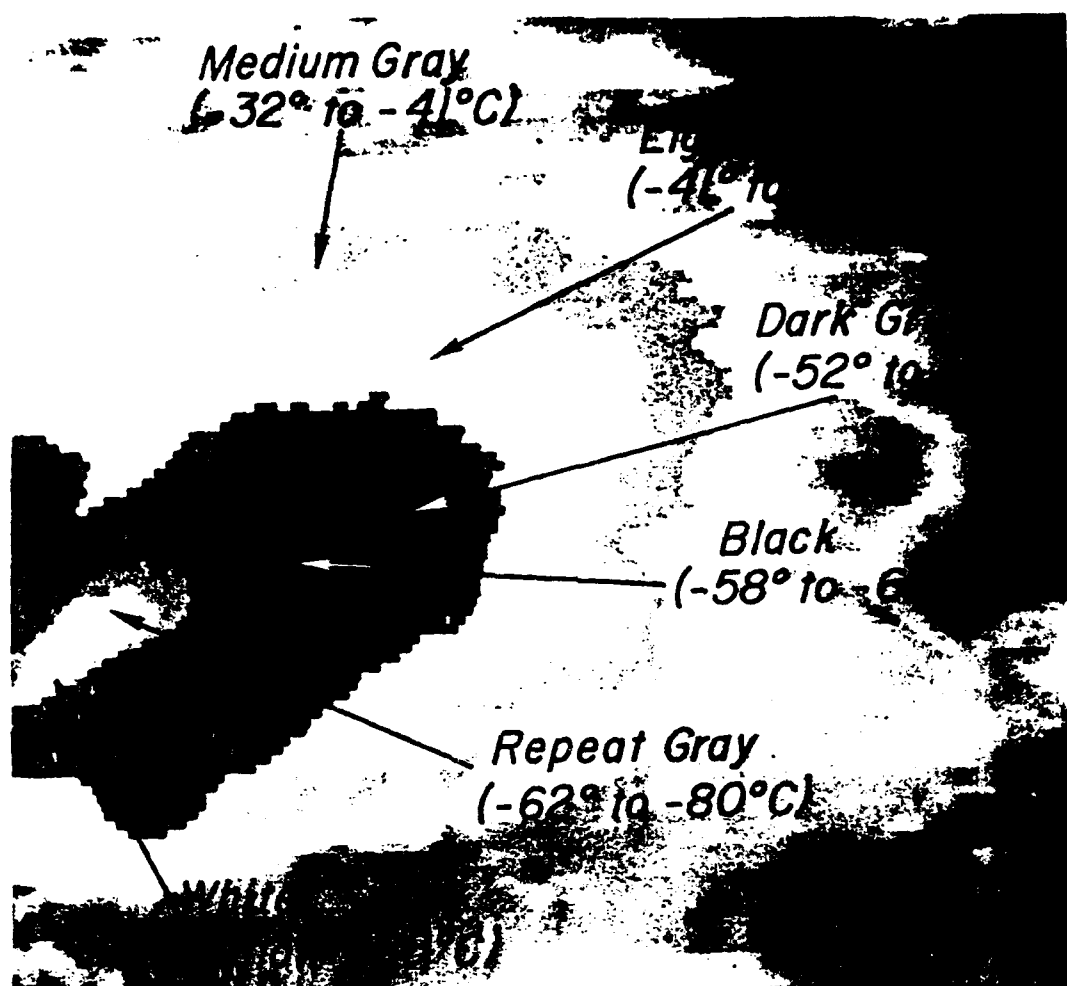


Fig. 2.4 MB enhancement curve used for analyzing GOES EIR pictures for MCC evaluation. This enhancement provides better definition of low- and mid-level clouds. Also allows good definition of very cold (overshooting) tops (temperatures between  $-63^{\circ}\text{C}$  and  $-80^{\circ}\text{C}$ ). Typically used for rainfall estimates. (Clark, 1983)

Using the general definition outlined by Maddox (1980) and the MB enhancement curve in Fig. 2.4, this storm fits the criteria for classification as a developing MCC. Specifically, the areal extent of the -32°C contour is greater than 100,000 km<sup>2</sup> (Oklahoma occupies 188,000 km<sup>2</sup>) and the areal coverage of the -52°C contour is greater than 50,000 km<sup>2</sup> (it easily covers half of Oklahoma). Finally, the most active part of the storm remains over Oklahoma (Fig. 2.3).

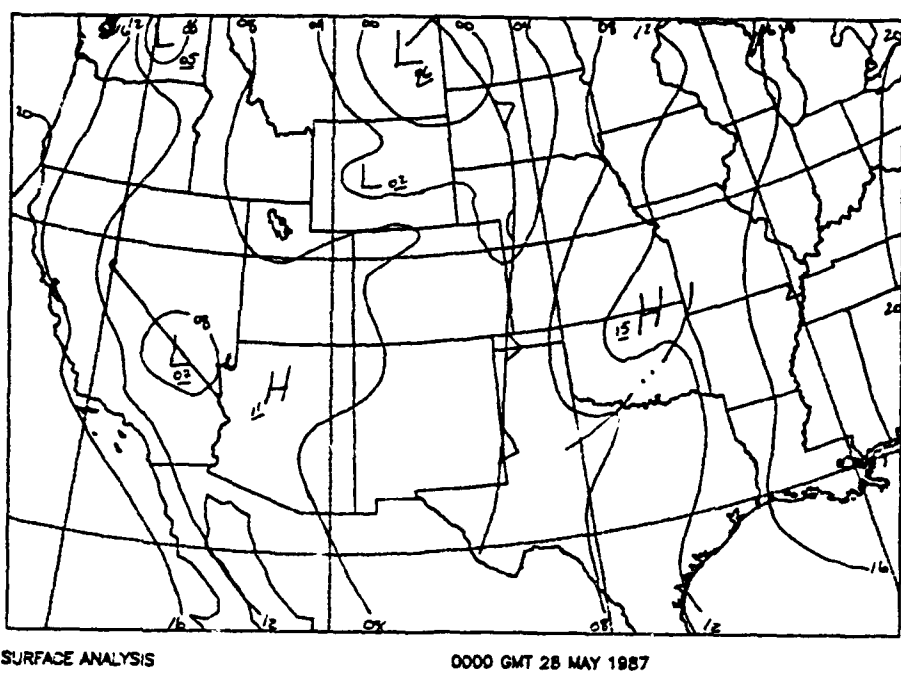
By 0000 GMT on 28 May 1987, a meso-high is evident at the surface behind the leading edge of the system (Fig. 2.5.a). According to Fujita (1955), this is typical of squall lines, which are a subset of mesoscale convective complexes. Examination of the 0031 GMT satellite picture (Fig. 2.5.b) shows two areas of activity over Oklahoma: one over the northeast corner and the other over the central portion of the state. The 0000 GMT skew-T diagram (Fig. 2.6) shows very strong directional shear (050° to 210°) below 500 mb and strong velocity shear (15 ms<sup>-1</sup> to 50 ms<sup>-1</sup>) below 700 mb. Between 400 mb and the tropopause (approximately 180 mb) there is a layer of strong, southerly flow. The temperature-dew point spread is very small (less than 4°C), indicating saturation throughout the column. Note the slight cooling at 850 mb and the slight drying of the layer around 700 mb. Figure 2.7 shows that the slight

cooling at 850 mb is due to a cold pool over Oklahoma City and southwestern Kansas, which is most likely due to evaporation. The cold pool at 850 mb corresponds to the location of the meso-high in Fig. 2.5.a, assuming the system is not perfectly vertically stacked. The high pressure perturbation at the surface is due to a hydrostatic pressure rise caused by colder, denser downdraft air intruding into the boundary layer (Fujita, 1959). Note the height falls over Oklahoma at 700 mb and 500 mb (Figs. 2.8.a and 2.8.b, respectively), which indicate convergence at those levels.

Fritsch (1988) mentions that an MCC typically forms on the anticyclonic (AC) side of the upper level jet. By forming on the right entrance region (AC side) of the jet, the MCC ensures itself of low level convergence and upper level divergence which, in turn, assures an exhaust mechanism in the vicinity of the jet entrance region. Inspection of Fig. 2.9 indicates that this is, indeed, the case over Oklahoma. Comparison with the wind speeds twelve hours earlier indicate that the 250 mb wind speeds have increased as much as 18%. The surface wind speeds over the same twelve hours are also unchanged, but the wind direction has changed due to the passage of the outflow boundary. This implies an increase in upward vertical motion (UVM) within the system over Oklahoma due to the upper level exhaust created by the stronger upper

level winds.

The following chapters will focus on the development stage of this storm from 2200 GMT (1600 CST) on 27 May 1987 through 0100 GMT (1900 CST) on 28 May 1987.



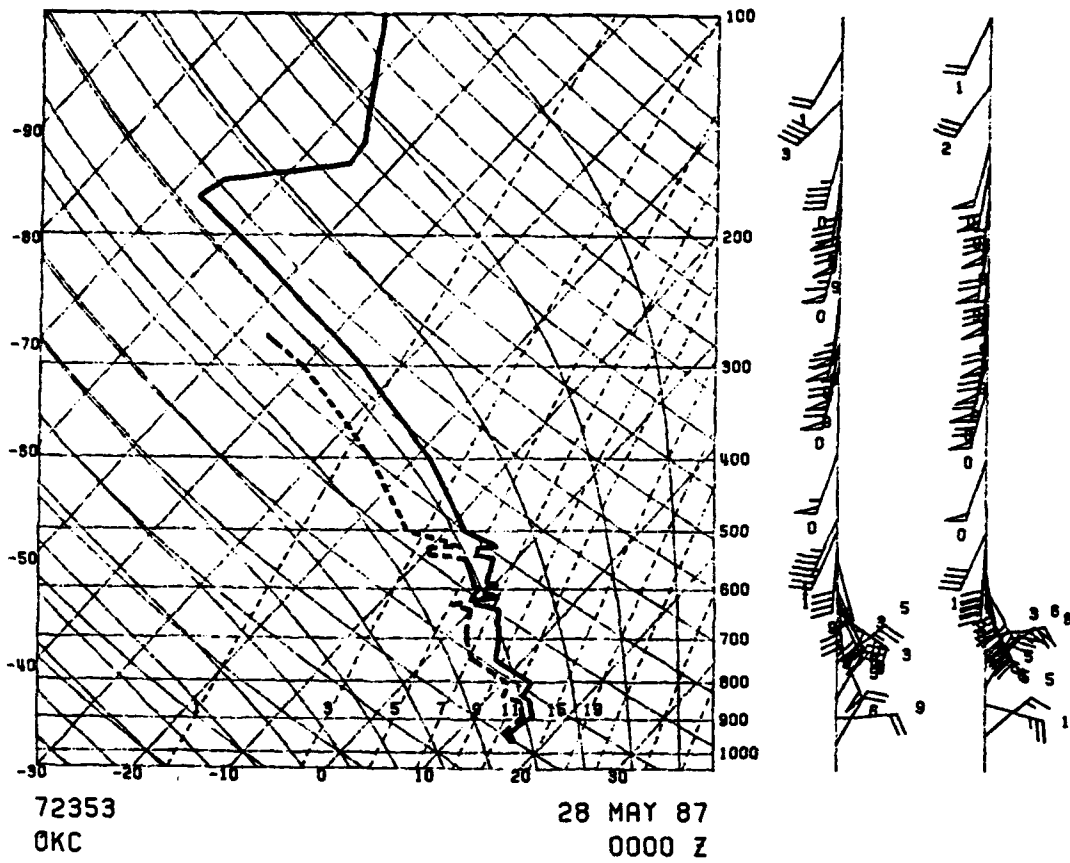


Fig. 2.6 0000 GMT 28 May 1987 skew-T log P diagram. Heavy solid line is environmental temperature and heavy dashed line is environmental dewpoint. Winds are given in  $\text{ms}^{-1}$ . Half barbs are  $5 \text{ ms}^{-1}$ , full barbs are  $10 \text{ ms}^{-1}$  and pennants are  $50 \text{ ms}^{-1}$ .

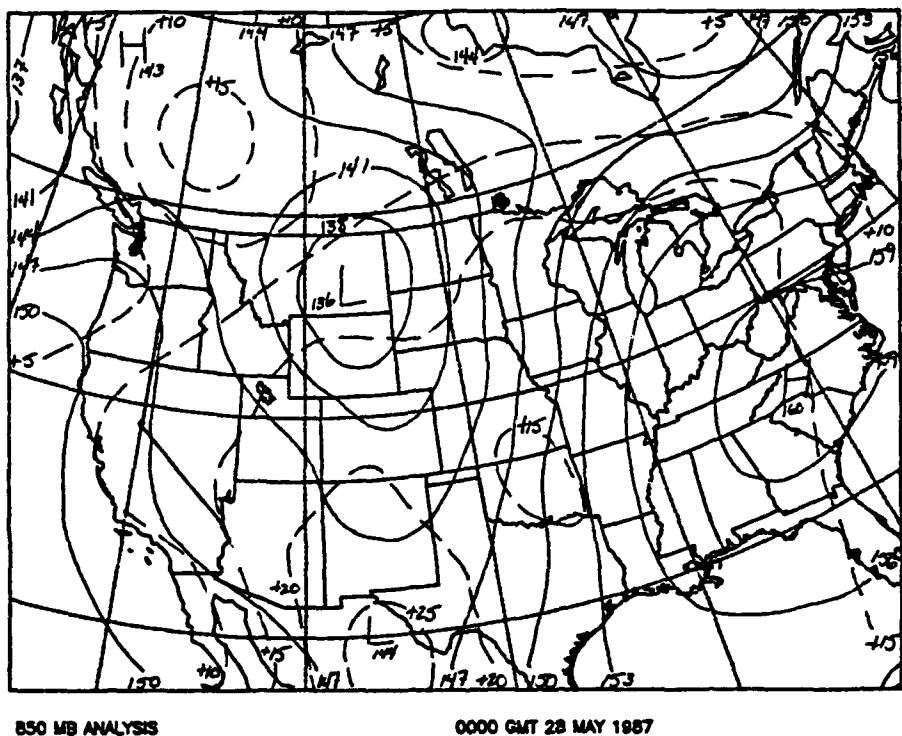
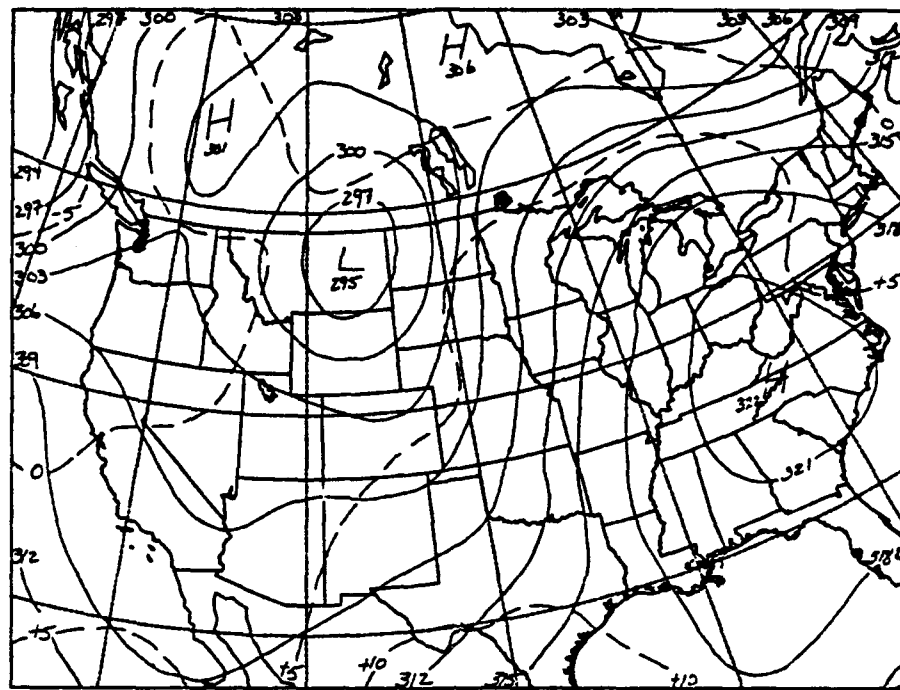
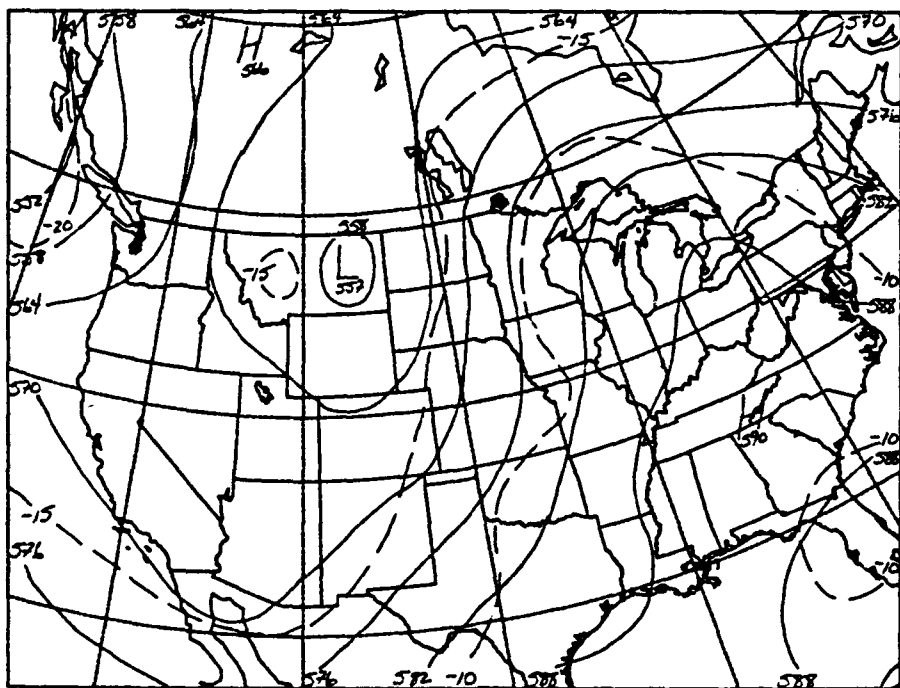


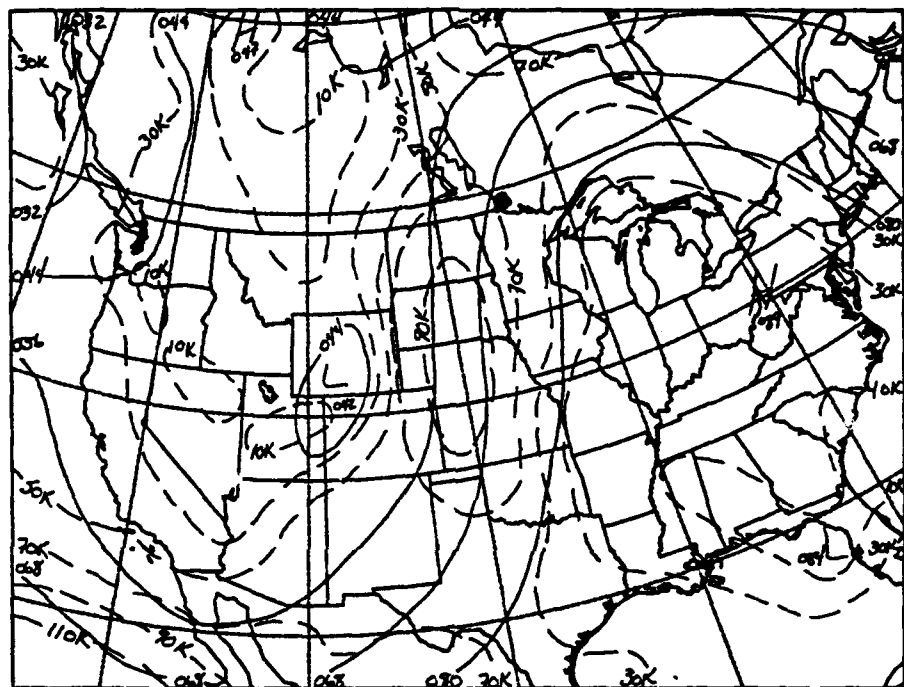
Fig. 2.7 0000 GMT 28 May 1987 850 mb analysis



700 MB ANALYSIS 0000 GMT 28 MAY 1987  
Fig. 2.8.a 0000 GMT 28 May 1987 700 mb analysis



500 MB ANALYSIS 0000 GMT 28 MAY 1987  
Fig. 2.8.b 0000 GMT 28 May 1987 500 mb analysis



## **CHAPTER III**

### **ANALYTICAL METHODS**

Two analytical methods were used in this investigation, the singularity extraction and the two-pass Barnes analysis methods. The data sets used for these analyses are described.

#### 3.1 Singularity Extraction

The data used in the singularity analysis was a series of Doppler radar volume scans from the National Severe Storms Laboratory's (NSSL) 10 cm radar in Norman, Oklahoma. The data was collected during the DOPLIGHT 87 weather data collection experiment in the Spring of 1987. The data was archived in the Universal Format (Barnes, 1980) and used in its unedited form throughout this investigation.

The Doppler velocity data is assumed to be usable beyond 5 km. Any signal within 5 km of the radar is assumed to be ground clutter and is ignored. The radar

data reaches out to 120 km, but only 100 km is used in this study.

In order for us to interpret the results, we must make several assumptions about the Doppler data. First, we assume the wind field is "quasi-steady." This means that in the several minutes required to do a volume scan, the temporal changes in the velocity field are negligible (Peace, et al., 1969). We also assume that there exists no system bias, since all Doppler radar observations are taken by the same radar (Doviak and Zrnic, 1984).

The singularity extraction is based on a scheme developed by Sasaki (1955) and Sasaki, et al. (1989). In the 1955 paper, Sasaki introduced singularity (vortex filament) theory to meteorology and applied it to the forecasting of typhoon tracks. The scheme described in the 1989 article utilized the Green's function theory of local symmetry and a variational extraction. The variational extraction is outlined in Appendix A. Figure 3.1 is a diagram of a singularity with local symmetry associated with a source (divergence). The radial velocity of the flow from a singularity point is symmetric relative to that point. The radial velocities on a concentric circle about a singularity point are the same. The radial velocity,  $V_r$ , is measured relative to the radar,  $R$ , along the beam,  $r$ .  $V_r$  can be measured

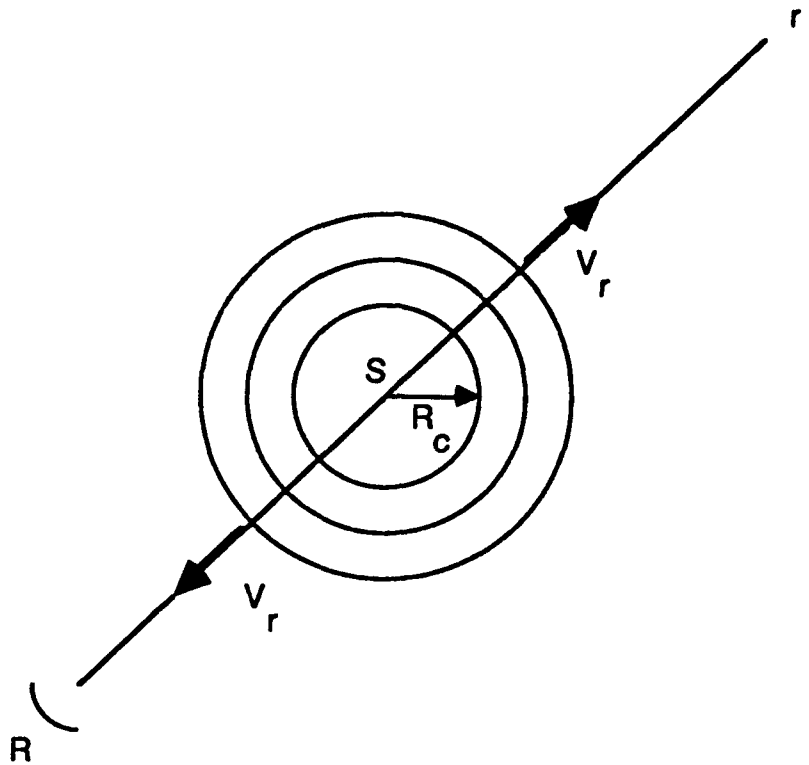


Fig. 3.1 Schematic diagram of a singularity and the local symmetry for a source (divergence). A sink (convergence) singularity is the same, only the arrows are reversed. (After Sasaki, et al., 1989)

similarly for the other concentric circles.

If we plot the radial velocity,  $V_r$ , at the intersection of each concentric circle along  $r$ , we obtain a Rankine combined velocity profile (Fig. 3.2). The inner portion of the profile is assumed to be a uniform intensity source, and as such, increases linearly with distance from the center:

$$V_r = C_1 r \quad (1)$$

The most probable physical mechanism for the inner portion of the profile to be linear with distance from the singularity point is viscosity. The outer portion of the profile is inversely proportional to the distance from the singularity point,  $S$ , (Lamb, 1932; Milne-Thomson, 1960; Wood and Brown, 1983):

$$V_r = \frac{C_2}{r} \quad (2)$$

The maximum velocity,  $V_m$ , occurs at the core radius,  $R_c$ . Once the maximum velocity has been determined, the constants,  $C_1$  and  $C_2$ , can be determined:

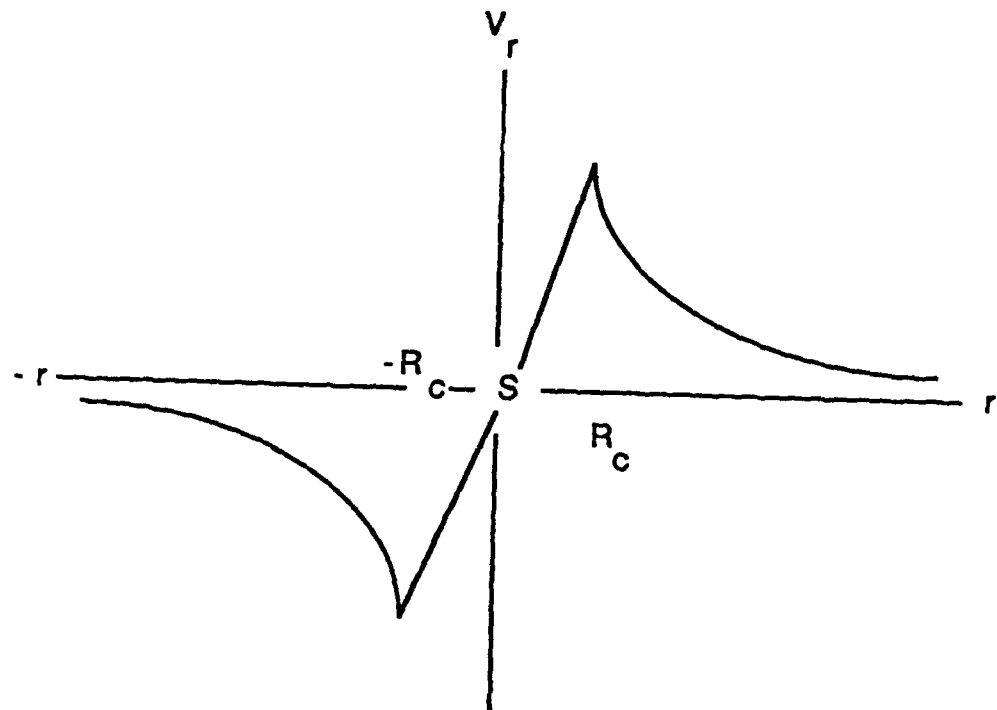


Fig. 3.2 Rankine combined velocity profile shows the radial distribution along the radar beam about a singularity,  $S$ .  $R_c$  is the core radius. (After Wood and Brown, 1983; Sasaki, et al., 1989)

$$C_1 = \frac{V_m}{r} \quad (3)$$

$$C_2 = V_m r \quad (4)$$

Since the Doppler radar radial velocities,  $V_r$ , are collected in both the negative  $r$  and positive  $r$  directions along the radar beam around the singularity point, S, we can determine the location and intensity by fitting the observed  $V_r$  to the theoretical  $V_r$  in Fig. 3.2 in a least-squares sense for each singularity point. Since the  $V_r$  observations represent an integrated effect of all singularity points, a variational method was originally employed in order to separate each singularity so that

$$\nabla \cdot V = \frac{\partial V_r}{\partial r} + \frac{1}{r} \left[ V_r + \frac{\partial V_\theta}{\partial \theta} \right] \quad (5)$$

$$= \frac{\partial V_r}{\partial r} + \frac{V_r}{r}$$

$$= 0$$

and continuity holds.

This means that we can model divergence as a series

of concentric circles about a source (singularity) and determine the strength of this source using (3) based on the radius of these circles (Rouse, 1961).

The actual computation scheme used in this study utilized a "short cut" of the above technique. We capitalized on the local symmetry of a source or sink singularity point. By focusing primarily on the symmetry about a singularity point, we can exploit the relatively large ( $O(10^{-2} \text{ s}^{-1})$ ) positive or negative values of the "signature" divergence calculated. By "signature" divergence values, we mean those values of divergence associated with storm-scale features (e.g., gust front).

Figure 3.3 shows the computation steps followed. The first step involves averaging the radial velocities over some set distance along the radar beam. In this particular case, we chose the averaging distance ( $R_c$ ) to be 1 km, which corresponds to seven gates of data. The core radius,  $R_c$ , was chosen to maximize the amount of information obtained about storm scale dynamics. Storm scale is on the order of 10-20 km with internal scales (rainshaft, tornado, etc.) of 1-2 km (Orlanski, 1975). Missing velocity values are flagged in the raw data and we ignore those particular gates. In order to maintain

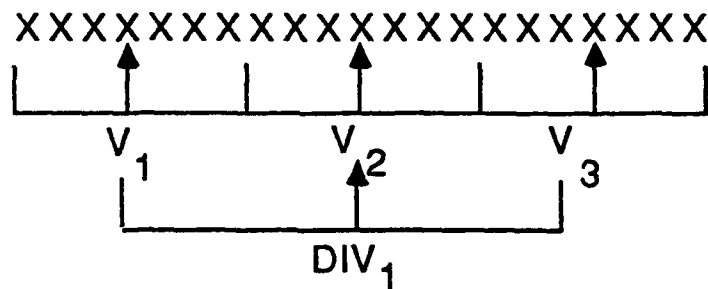


Fig. 3.3 Steps used in the singularity computation. Seven gates of velocity measurements (X) are averaged and the average velocity is written to the center gate of the seven ( $V_1$ ,  $V_2$  and  $V_3$ ). The divergence singularities are calculated using (5).

the representativeness of the averaged radial velocities, we further require that at least five gates be available in each seven gate group for averaging. Averaged gates with less than five gates of usable data are flagged as missing data. In addition, velocities less than  $1 \text{ ms}^{-1}$  are ignored, because they fall within the noise domain of the radar.

Noise is eliminated from the singularities using a "common sense" approach. Each velocity used in the averaging is checked against the average value. The average value is flagged as missing data if any one of the velocities differs from the average value by more than  $10 \text{ ms}^{-1}$ . The assumption in this case being that variations greater than  $10 \text{ ms}^{-1}$  from the average value constitute significant noise. This reduces the occurrence of edge effects appearing in the analysis.

Once the average radial velocity is computed, it is written to the central point of the group of seven ( $V_1$ ,  $V_2$  and  $V_3$  in Fig. 3.3). The divergence singularity is then computed via the centered difference

$$\frac{V_{i+2} - V_i}{2(\Delta R)} = DIV_i \quad (6)$$

The value of  $DIV_i$  is then written to the same location as

$v_{i+1}$ . The next value of the divergence singularity is then computed using  $v_{i+1}$  and  $v_{i+3}$ . The remaining divergence singularities along the radar beam are computed similarly, stepping along the radar beam one averaged velocity value at a time. If one of the averaged values is flagged as missing data, the resulting value of the divergence singularity is not written to the plot file. Further, divergence singularity values less than a threshold provided by the user are ignored and not written to the plot file. This is done to conserve the amount of memory used and also reduces the amount of computer time used.

Processing a single sweep using this method has proven very quick and efficient. On a day when the computer has a maximum number of users online, the actual CPU time of the divergence singularity computation is approximately 30 seconds. Complete processing of the graphical image takes about three minutes from start to finish. The slow parts of the process are the search and plot portions of the algorithm, with the search routine taking the longest time overall. We used an NSSL subroutine that reads the data in the Universal Format one record (beam) at a time. The speed of the graphical output depended on whether the graphics were sent to a terminal or to a paper plotter, with the latter being the slowest. Normally, the whole process takes only a few

seconds. This is very beneficial, because we can (theoretically) take the data stream directly from the radar and display the singularities in real-time.

### 3.2 Precipitation Analysis

The rainfall recorded throughout the state of Oklahoma from 1600 CST to 2000 CST 27 May 1987 was objectively analyzed in hourly blocks using a two-pass Barnes analysis (Koch, et al., 1983). Figure 3.4 shows the locations of the raingages and the outline of the 200 km by 200 km analysis grid used. The derivation of the parameters used in this analysis is included in Appendix B.

The rainfall data used in this analysis consisted of hourly observations at 29 raingages spread over 118,000 km<sup>2</sup> in central Oklahoma (NOAA, 1987a). An analysis was done for each hour of accumulation from 1600 CST to 2000 CST 27 May 1987.

The errors associated with raingage measurements of rainfall are well documented (Brandes and Wilson, 1988). Primary sources of error are gage wetting, gage inclination, splash into or out of the gage, evaporation and airflow around the gage. Much of the measurement error is associated with turbulence and increased velocities about the gage orifice (Larson and Peck, 1974). An estimated undermeasure of rainfall in strong

outflow regions of thunderstorms may be as high as 20-40% (Brandes and Wilson, 1988). For these reasons, the precipitation analysis was used more as an indicator of the areal extent of the precipitation, rather than a quantitative measure. The precipitation analysis is depicted with an infimum of 6 mm in order to show the areal extent of the hourly rainfall accumulation.

Using the precipitation analysis in conjunction with the divergence singularity analysis brings up the question of the difference in scales between the two (10 km and 2 km for precipitation and singularities, respectively). Based on the above arguments, the differences in scale are unimportant provided we limit our discussion of the relationship between the two fields to their relative locations, rather than as absolute relationships.

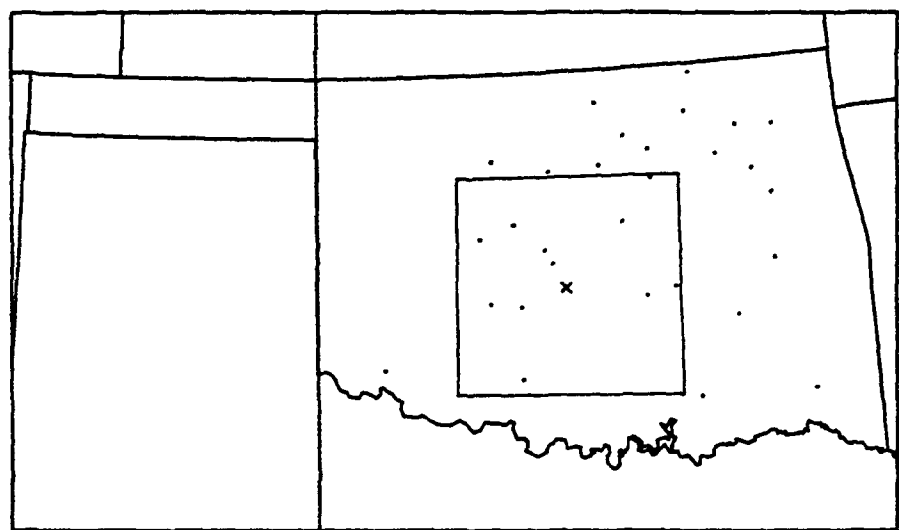


Fig. 3.4 Map of Oklahoma showing the locations of the 29 raingages used in the precipitation analysis and the location of the 200 km X 200 km analysis grid. The radar is marked as an X at the center of the grid.

## **CHAPTER IV**

### **RESULTS AND DISCUSSION**

The singularity analysis of the Doppler radar velocities can be broken down into three major categories. While each category is unique, each is interrelated with the other two.

The three categories are broken down by order of magnitude and signature. Storm features are characterized by gust front signatures and singularity magnitudes from  $2 \times 10^{-2} \text{ s}^{-1}$  to  $8 \times 10^{-3} \text{ s}^{-1}$ . Background features are characterized by widespread singularities and singularity magnitudes less than  $8 \times 10^{-3} \text{ s}^{-1}$ . Folded features are characterized by convergence/divergence couplets and singularity magnitudes greater than  $2 \times 10^{-2} \text{ s}^{-1}$  when the Nyquist velocity is  $34 \text{ ms}^{-1}$ .

Each sweep at a given elevation angle traces out a cone shape in the volume. For ease of presentation, this cone shape has been projected onto a flat surface. The height of the cone surface at a given range,  $r$ , from the radar is given by (Doviak and Zrnic, 1984):

$$h = [r^2 + a_e^2 + 2ra_e \sin \theta_e]^{1/2} - a_e \quad (6)$$

Where:  $a_e$  = effective curvature of the earth

$\theta_e$  = elevation angle of the radar

Figure 4.1 shows the approximate heights for the elevation angles in a volume scan using (6).

Since the centered differences are being computed on a sloped surface, the divergence singularity is not pure divergence. What is actually being computed is a combination of divergence and deformation. We have assumed that the deformation is the same order of magnitude as the divergence and is, therefore, mathematically unseparable. "Divergence singularity" will be used throughout the following discussion to mean the singularity calculated on the sloped surface and not the "true" divergence, which is calculated on a horizontal plane.

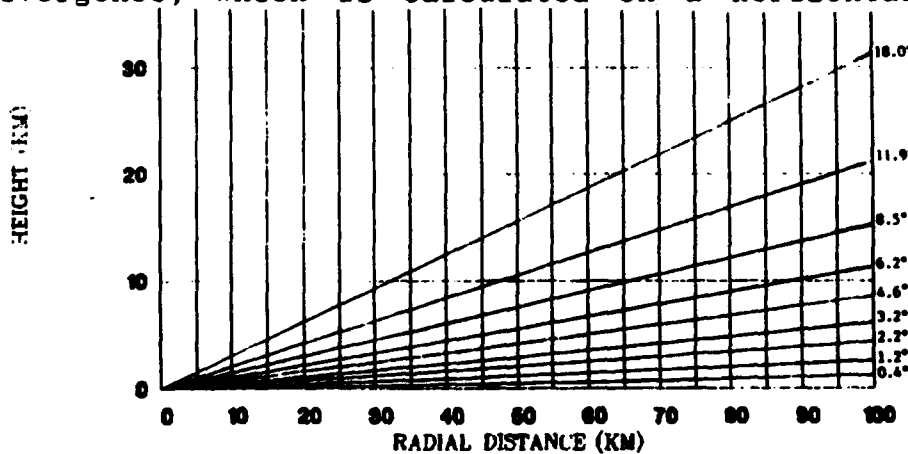


Fig. 4.1 Scan heights for each elevation angle.  
(Frashier, 1990)

#### 4.1 Meteorological Features

The 0.4° elevation (low-level) sweep shows a few scattered singularities through many of the earliest volume scans. At 233256 GMT (173256 CST) 27 May 1987 a series of convergence singularities resembling an arc appear (Fig. 4.2.a). Figures 4.2.b and 4.2.c are the associated velocity and reflectivity data at 233256 GMT (173256 CST) 27 May 1987. These singularities range from  $1.06 \times 10^{-2} \text{ s}^{-1}$  in the northernmost, or head, portion of the arc to  $8 \times 10^{-3} \text{ s}^{-1}$  in the southernmost, or tail, of the arc. The maximum divergence singularity value appears at 7.5 km from the radar, which is about 52 m above the surface.

As time marches on, the gust front becomes more obvious as an arc of singularities to the east of the radar (Figs. 4.3 and 4.4). By the time the gust front is identified at 1802 CST, the singularity analysis shows the gust front becoming more diffuse toward the tail.

During the time just before the gust front first appears in the low-level singularity analysis, Chickasha (CHK on the figures) recorded 27.94 mm (1.1 in) of rainfall between 1615 CST and 1730 CST (NOAA, 1987b). Fort Cobb (FTC on the figures) had recorded 40.64 mm (1.6 in) of rainfall between 1545 CST and 1645 CST (NOAA, 1987b). Just before and just after the gust front was

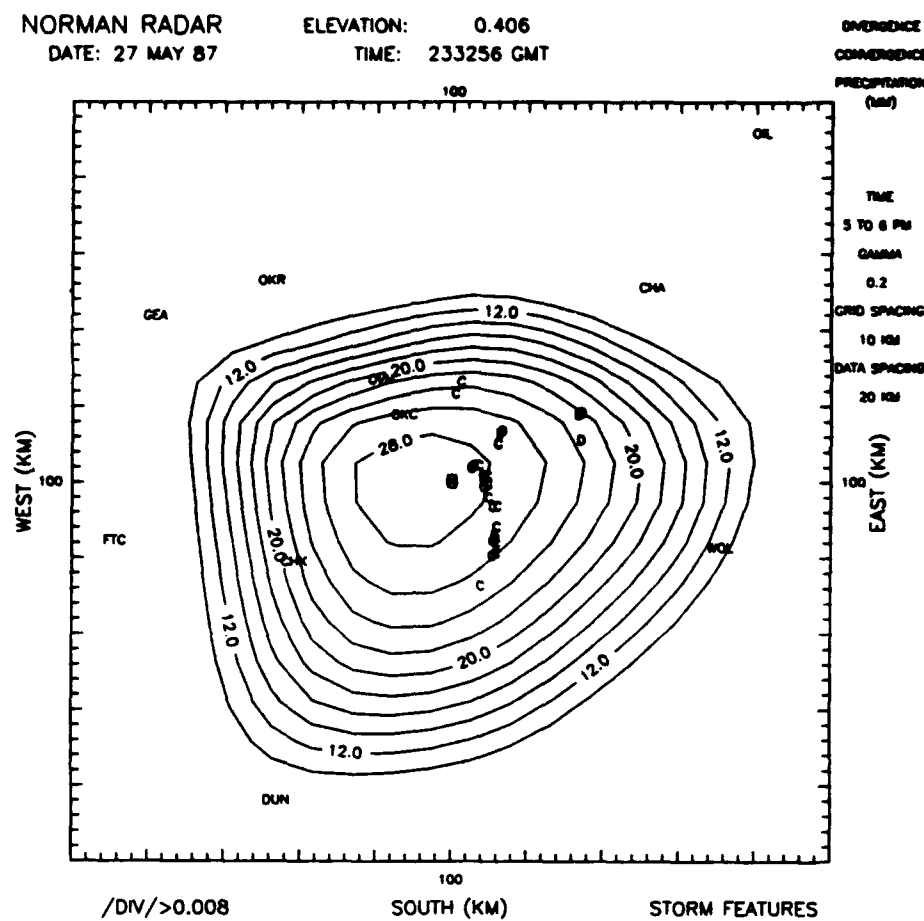


Fig. 4.2.a 233256 GMT (173256 CST) 27 May 1987  
singularity analysis. Convergence singularities are indicated as a C and divergence singularities are indicated as a D. The radar is located at the center (circled X). The contours are millimeter of precipitation ranging upward from 10 mm in 2 mm increments. The time period of the rain accumulation is identified under "TIME" and is given as CST. The constants used for the precipitation analysis are listed below "TIME." The type of singularity analysis is given in the lower right corner and associated thresholds are given in the lower left corner. The raingages are identified according to the nearest city or landmark: Chandler (CHA), Chickasha (CHK), Duncan (DUN), Fort Cobb (FTC), Geary (GEA), Lake Overholser (OVH), Oilton (OIL), Okarche (OKR), Oklahoma City Weather Service Office (OKC) and Wolf (WOL).

# Best Available Copy

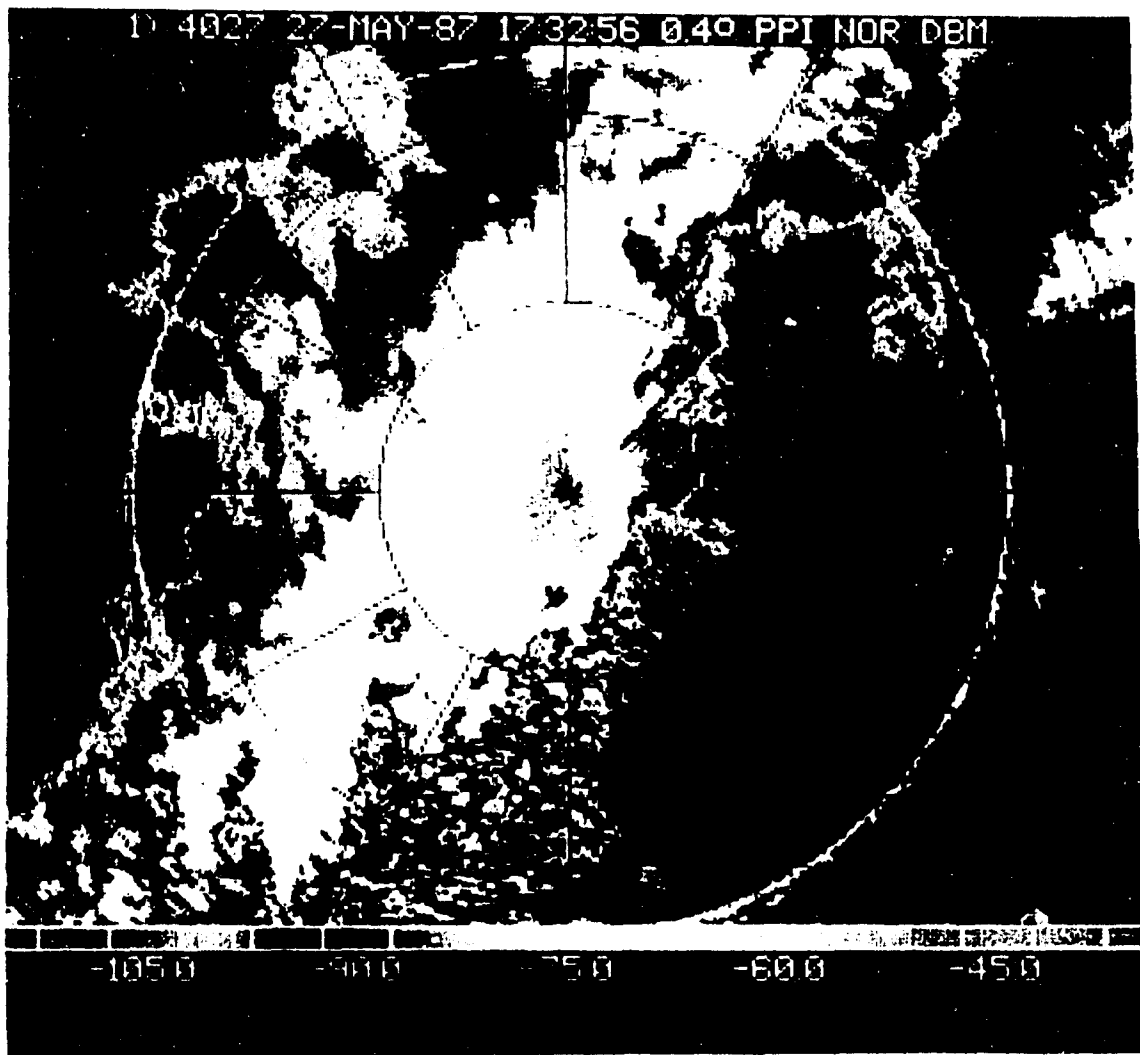


Fig. 4.2.b 233256 GMT (173256 CST) 27 May 1987 reflectivity. Range rings are 50 km apart and the ring outside the 100 km ring is the extent of the first trip echo. Units are in dBZ (DRM-10, 100 dBZ, DRFM-10; 8 ms in  $\text{g m}^{-3}$ ) (Battan, 1973).

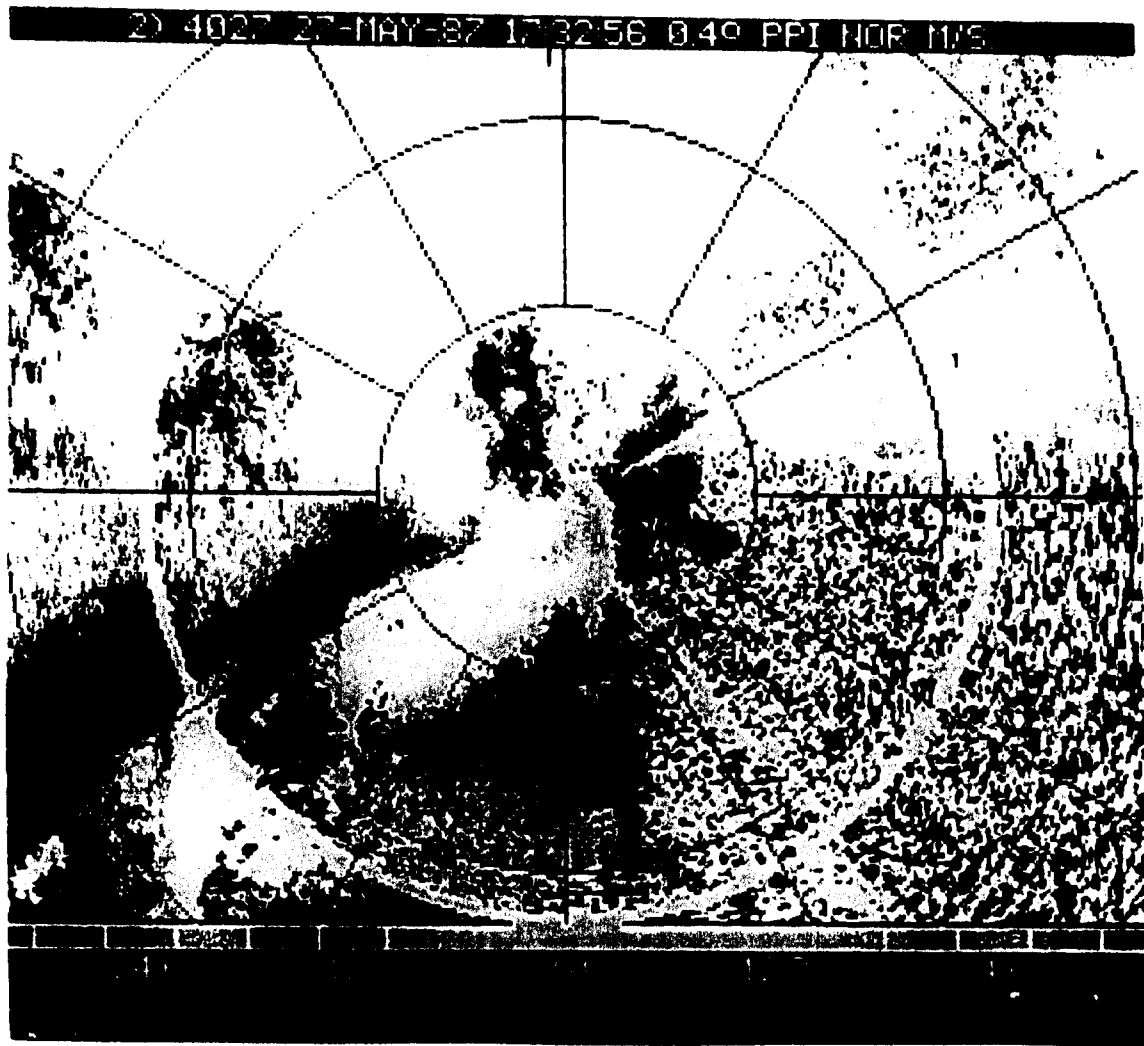


Fig. 1.2.c 233256 GMT (173256 CST) 27 May 1987 velocity. Range rings are the same as for Fig. 4.2.b. Units are in  $\text{ms}^{-1}$ . According to convention, positive values are velocities away from the radar and negative values are velocities towards the radar (Doviak and Zrnic, 1984).

identified (1745 CST to 1815 CST) Lake Overholser (OVH on the figures) recorded 30.48 mm (1.2 in) of rainfall (NOAA, 1987b). The National Weather Service at Oklahoma City (OKC on the figures) also reported 40.13 mm (1.58 in) of rainfall between 1700 CST and 1800 CST (NOAA, 1987b). This suggests that the rainband most likely associated with the gust front identified at 1802 CST was moving from southwest to northeast. Inspection of the singularity plots (Figs. 4.2, 4.3, 4.4 and 4.5) shows the head of the gust front moving toward the northeast. This implies that the progression of the gust front head can be used to infer the general direction of the heaviest rainfall.

Earlier work (Auer, et al., 1969) reveals that the gust front associated with an intense, quasi-steady thunderstorm usually leads the main precipitation core by 5 or 6 km. When the gust front is very far in front of the precipitation core, the supply of boundary layer air is cut off, causing the decay of the thunderstorm (Moncrieff and Miller, 1969; Browning, 1982). This is apparently what happened to this cell. The gust front is approximately 100 km ahead of the heaviest rainfall in Fort Cobb and Chickasha at 1745 CST. The position of the gust front at 1802 CST is about 45 km ahead of the objectively analyzed rainfall center (Fig. 4.5). Over the course of the next hour, the gust front influences

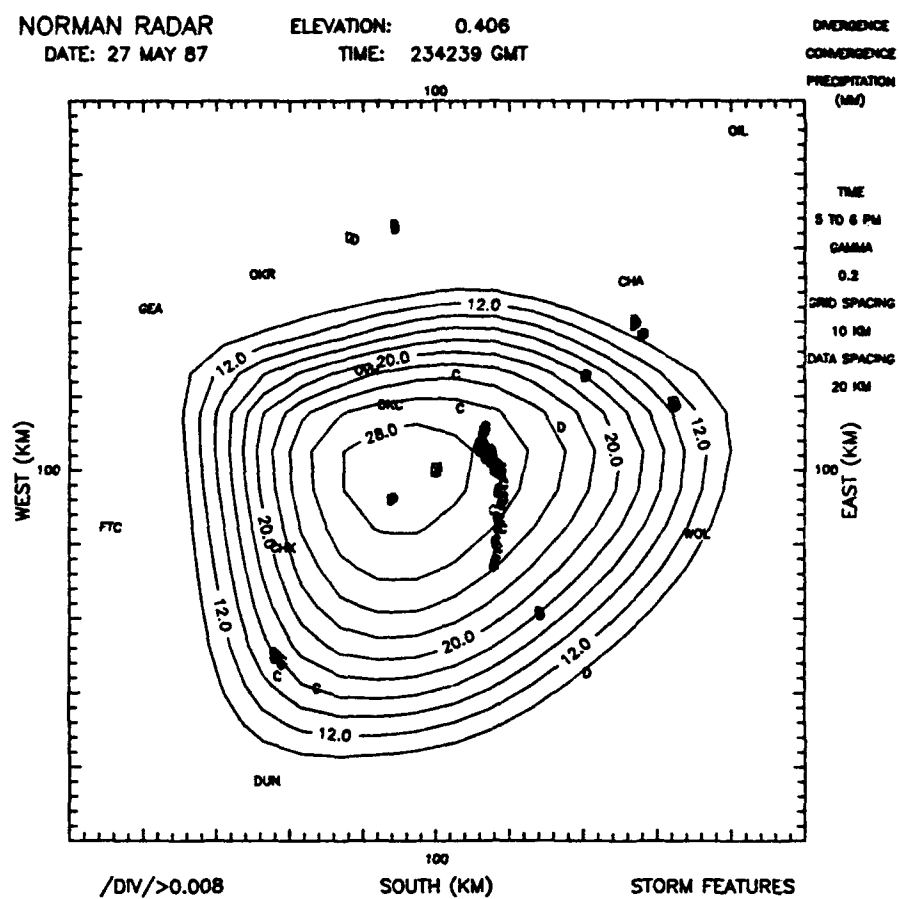


Fig. 4.3 Same as Fig. 4.2.a only for 234239 GMT (174239 CST) 27 May 1987.

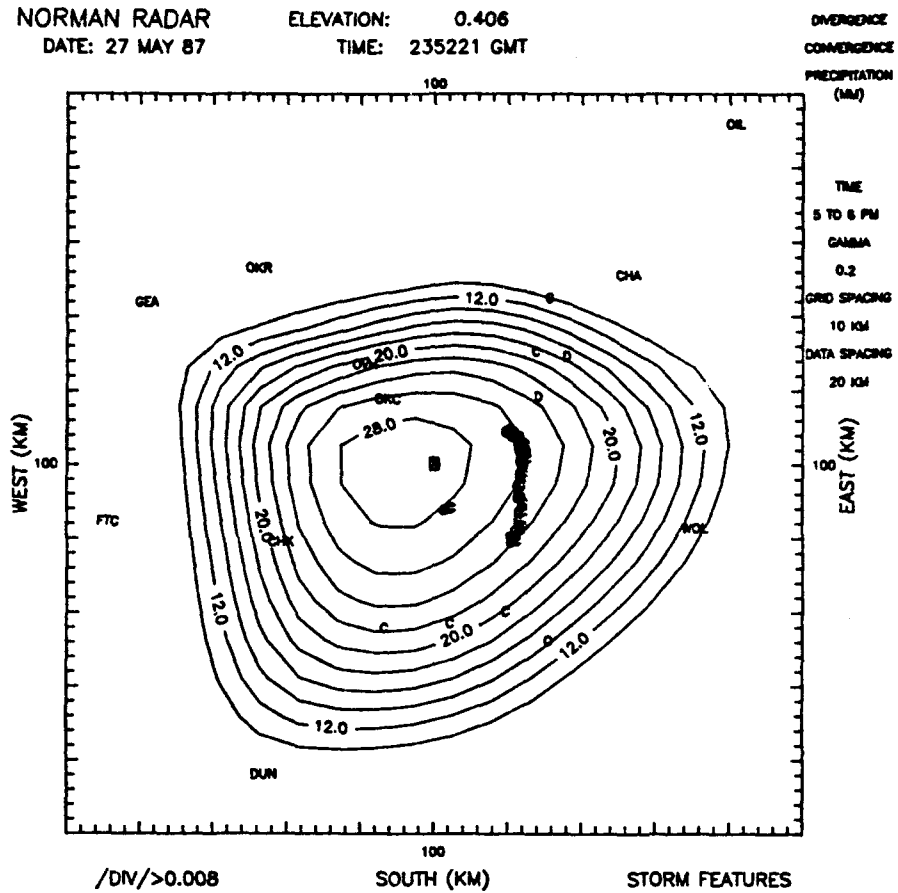


Fig. 4.4 Same as Fig. 4.2.a only for 235221 GMT (175221 CST) 27 May 1987

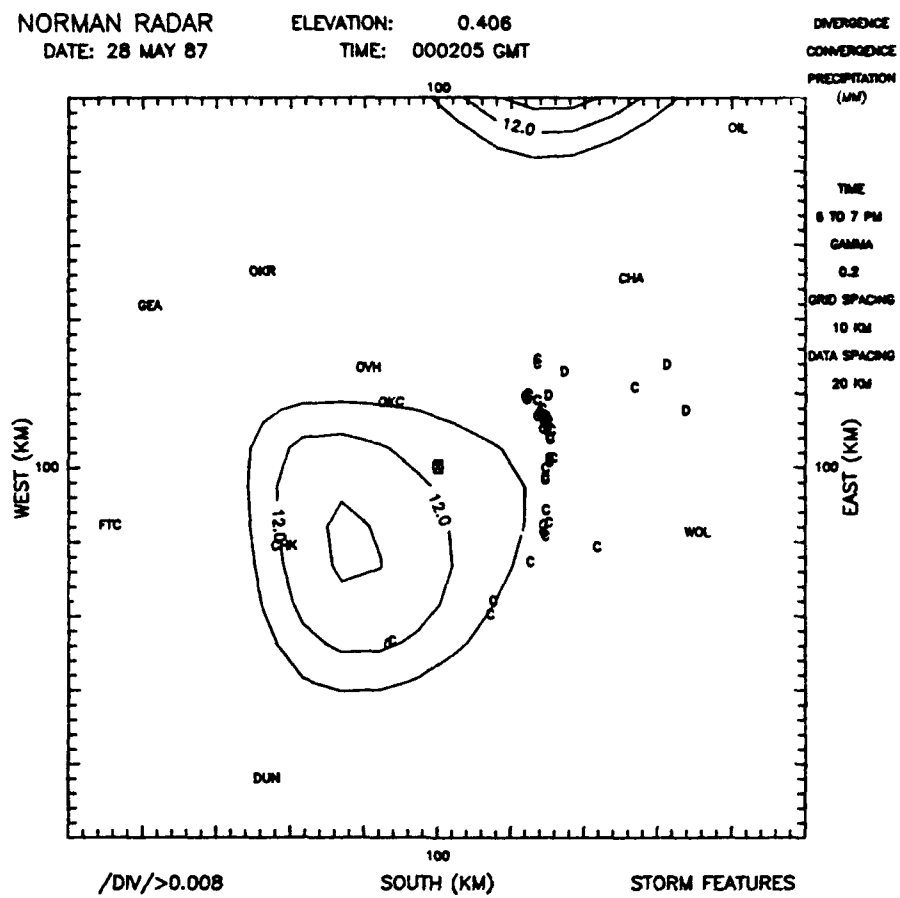


Fig. 4.5 Same as Fig. 4.2.a only for 000205 GMT (180205 CST 27 May 1987) 28 May 1987

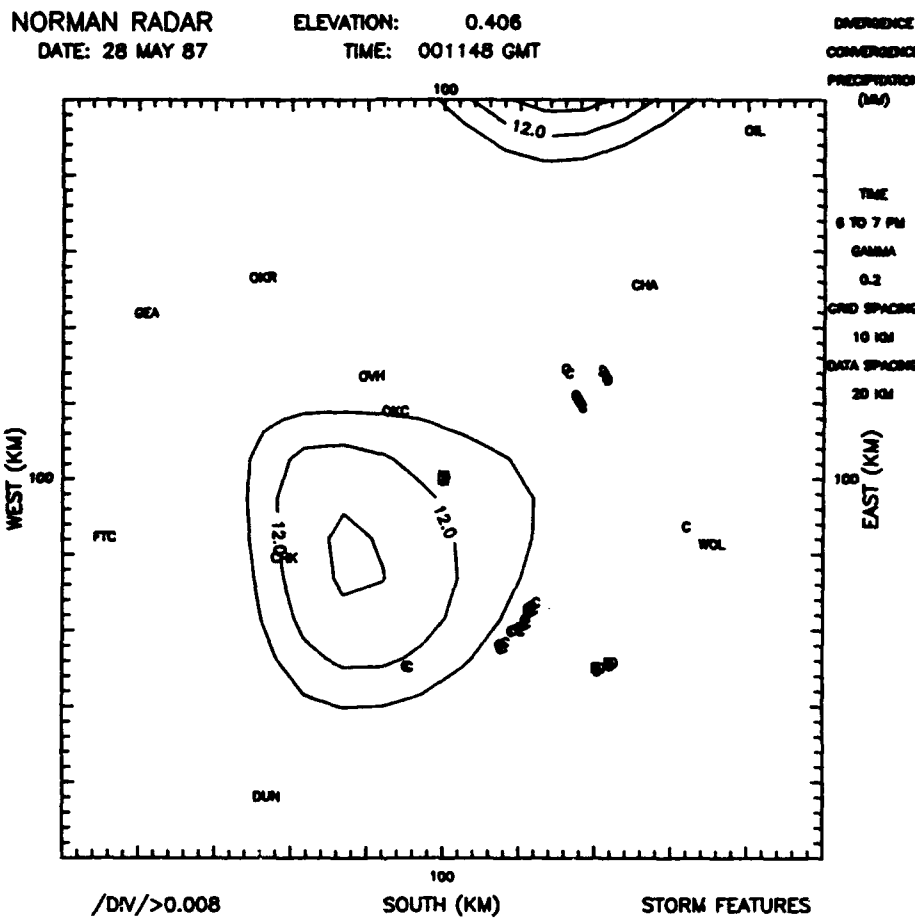


Fig. 4.6 Same as Fig. 4.2.a only for 001148 GMT (181148 CST 27 May 1987) 28 May 1987

the increase of activity to the northeast of the radar and the decrease of activity to the southwest (Fig. 4.6).

Examination of the volume scans shows how the line of convergence singularities works its way down through the boundary layer. The gust front is an identifiable feature in the 232618 GMT (172618 CST) 27 May 1987 analysis (Fig. 4.7). The strongest convergence singularity value is  $1.1 \times 10^{-2} \text{ s}^{-1}$  at this point. By the time the gust front appears in the low-level sweep, the convergence singularity value has increased to  $1.3 \times 10^{-2} \text{ s}^{-1}$  and the line has moved east (Fig. 4.8). Ten minutes later, the convergence singularity value has increased to  $1.7 \times 10^{-2} \text{ s}^{-1}$  (Fig. 4.9). Eight minutes before the gust front is identified, the line of convergence singularities shows signs of dissipating at  $3.09^\circ$  elevation (mid-level) and the value of the convergence singularity decreases to  $1.5 \times 10^{-2} \text{ s}^{-1}$  (Fig. 4.10).

These results show that we can identify a gust front at a higher elevation ( $3.09^\circ$ ) and almost 40 minutes before it is identified in the raw low-level data. Also, about the time the gust front is identifiable using the singularity analysis, the heaviest rainfall is just ending in Chickasha, 50 km west-southwest of the gust front.

From earlier work (Sasaki and Baxter, 1982) we know that a gust front builds downward through the atmosphere

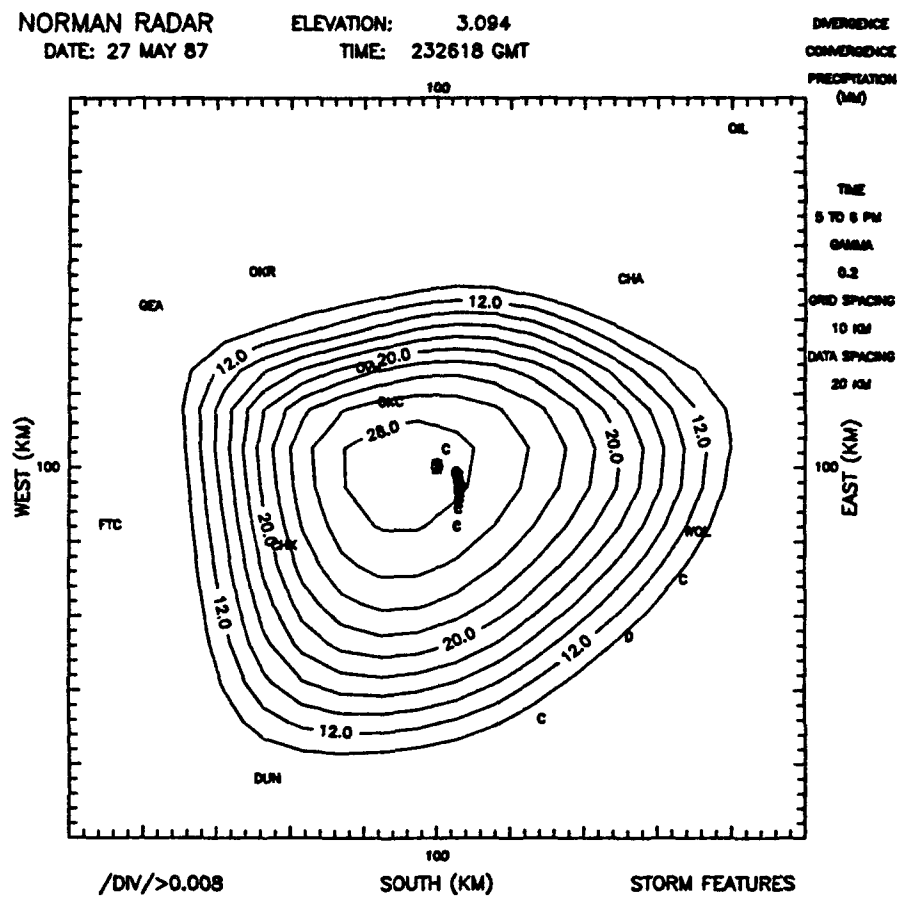
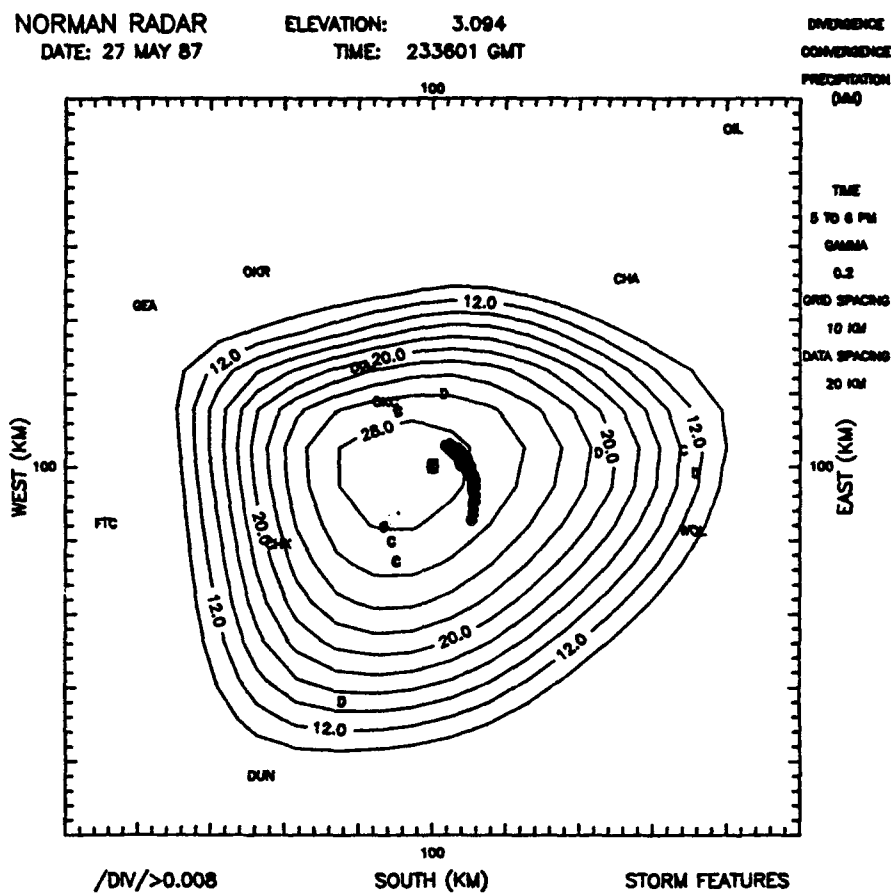


Fig. 4.7 Same as Fig. 4.2.a only for 232618 GMT (172618 CST) 27 May 1987



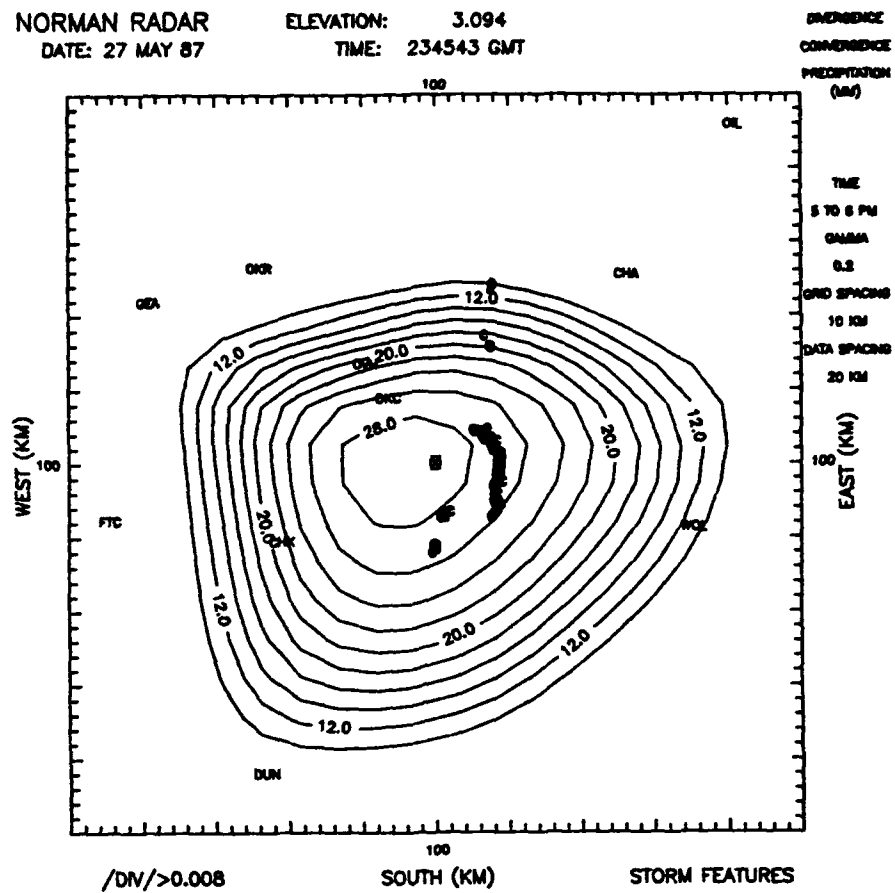


Fig. 4.9 Same as Fig. 4.2.a only for 234543 GMT (174543 CST) 27 May 1987

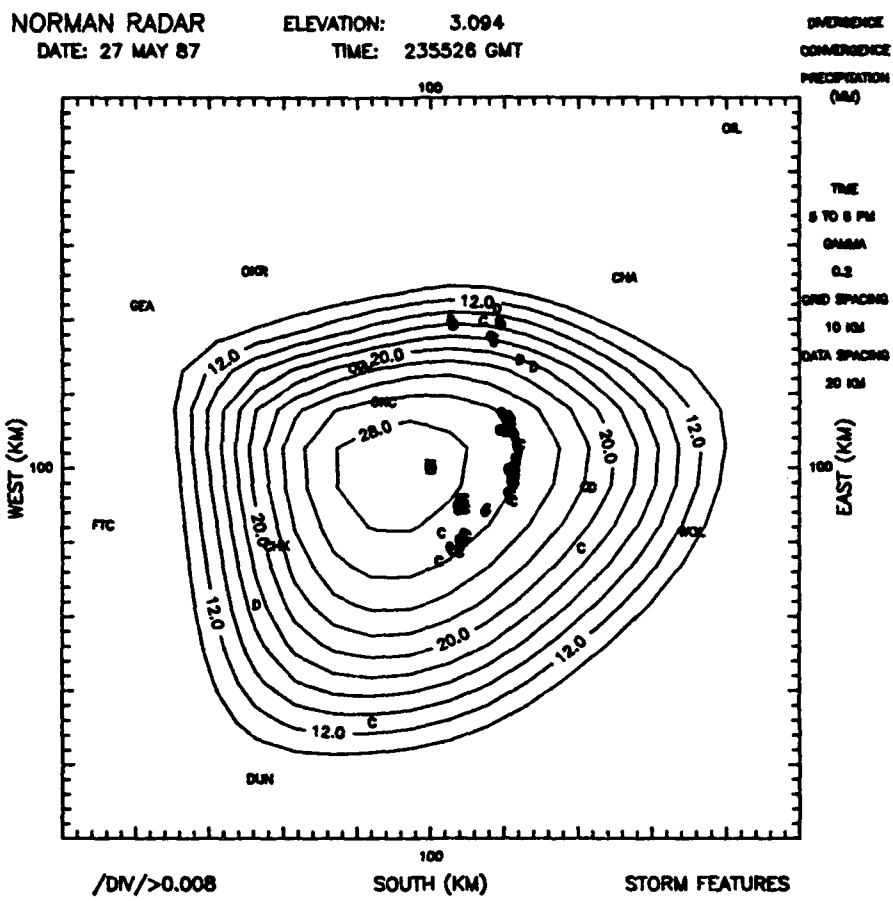


Fig. 4.10 Same as Fig. 4.2.a only for 235526 GMT (175526 CST) 27 May 1987

and that the parcel maintains its horizontal momentum from the higher level. If we can determine a simple way to estimate the velocity of the gust front winds when the singularity analysis first displays the gust front signature, then a warning can be issued for a particular area and time.

#### 4.2 Background Features

The background divergence singularities begin at  $-5.05 \times 10^{-5} \text{ s}^{-1}$  at the beginning of the data at low-levels and becomes more negative (convergent) over time. At 232439 GMT (172439 CST) 27 May 1987 the average background divergence becomes positive (Fig. 4.11). This particular analysis shows some very interesting features. The orientation of the divergence singularities and convergence singularities close to the radar and to the southwest suggest a general location for the downdraft. The location of the line of convergence singularities (gust front) and the line of divergence singularities to the northeast of the radar suggest that this cell could possibly be modeled like a squall line: divergence ahead of the advancing line of convergence and the gust front (Fig. 4.12). The line of divergence ahead of the gust front in Fig. 4.12 is due to the ascending air just ahead of the advancing outflow (Sasaki and Baxter, 1982).

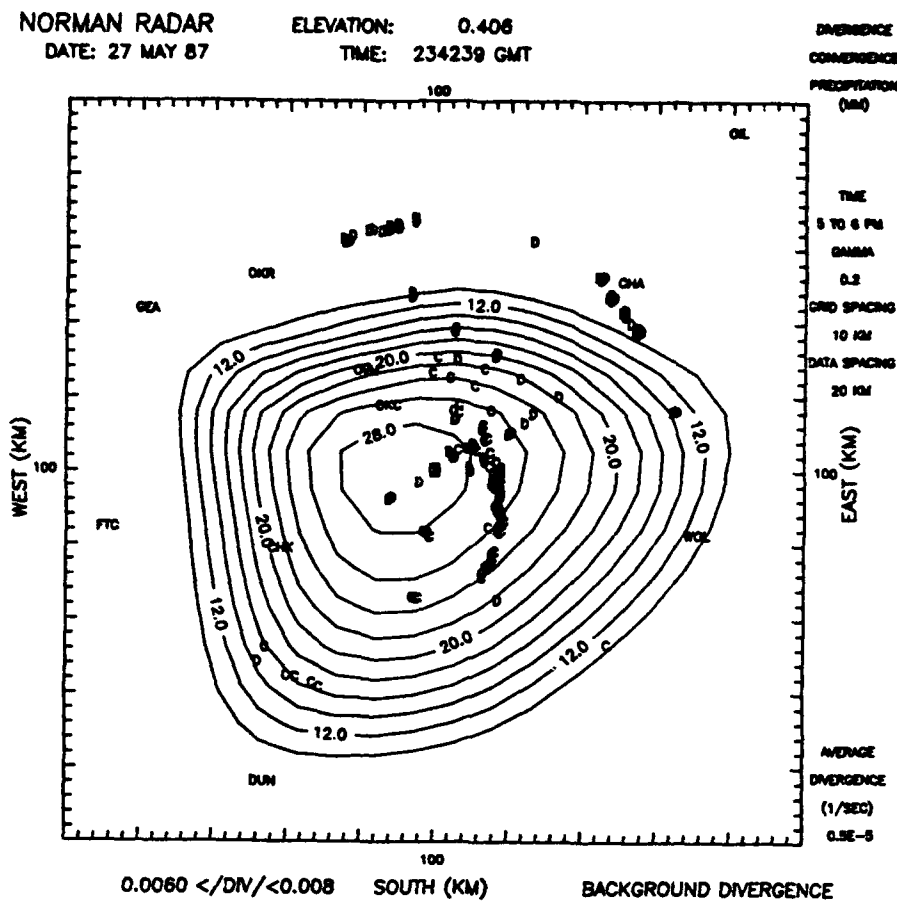


Fig. 4.11 Same as Fig. 4.2.a only for 234239 GMT (174239 CST) 27 May 1987

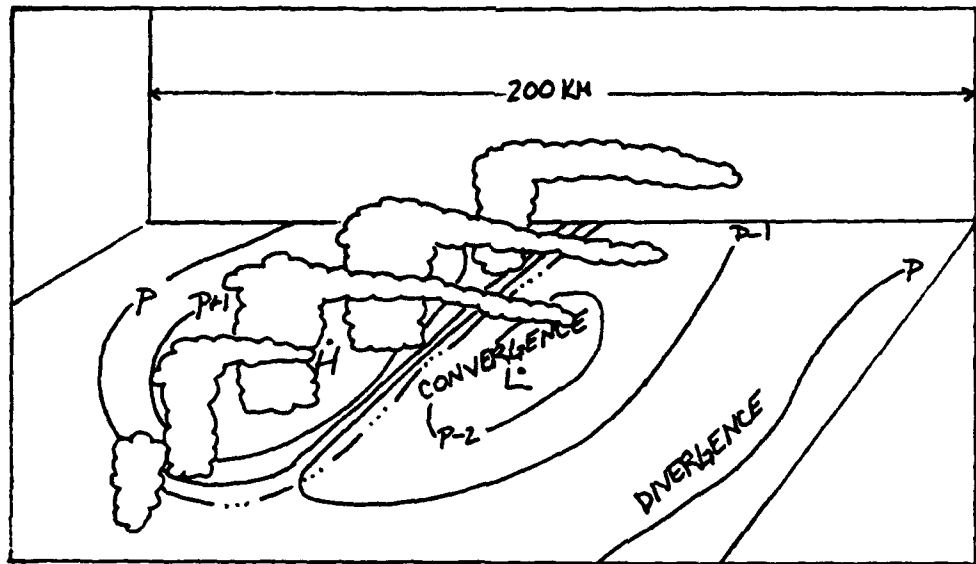


Fig. 4.12 Model of a squall line showing the location of the gust front, the meso-high to the rear of the gust front, the convergence zone ahead of the gust front and the divergence zone ahead of the convergence zone. (After Schaefer, et al., 1982)

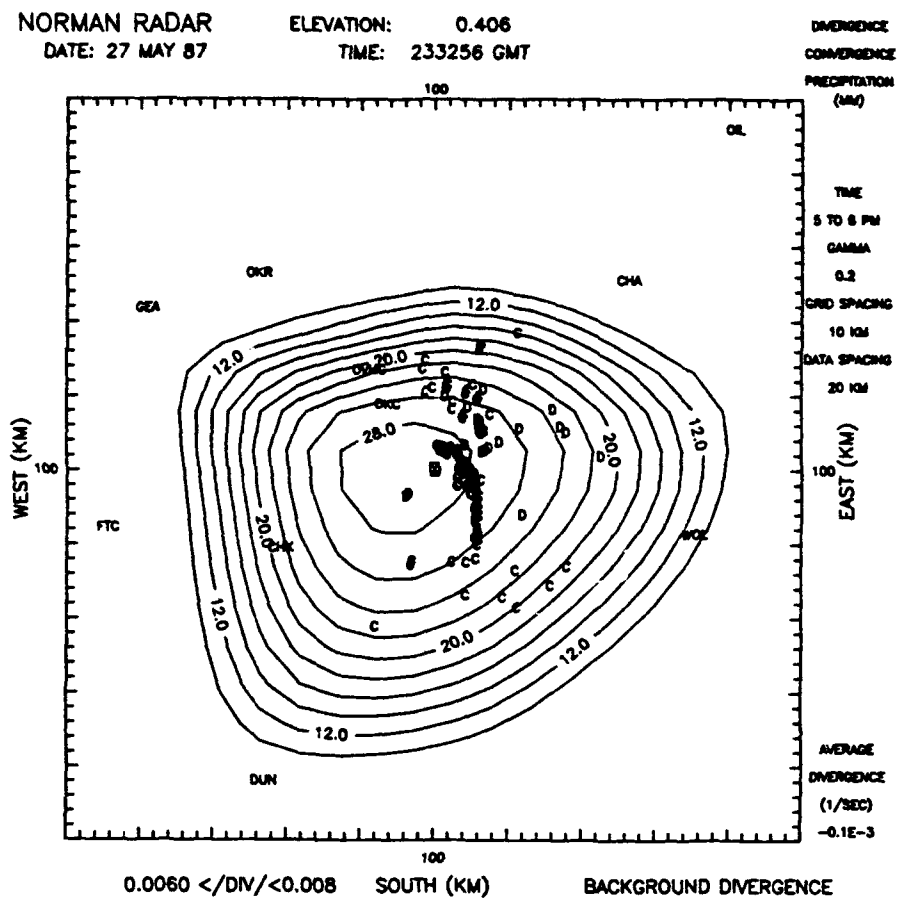


Fig. 4.13 same as Fig. 4.2.a only for 233256 GMT (133256 CST) 27 May 1987

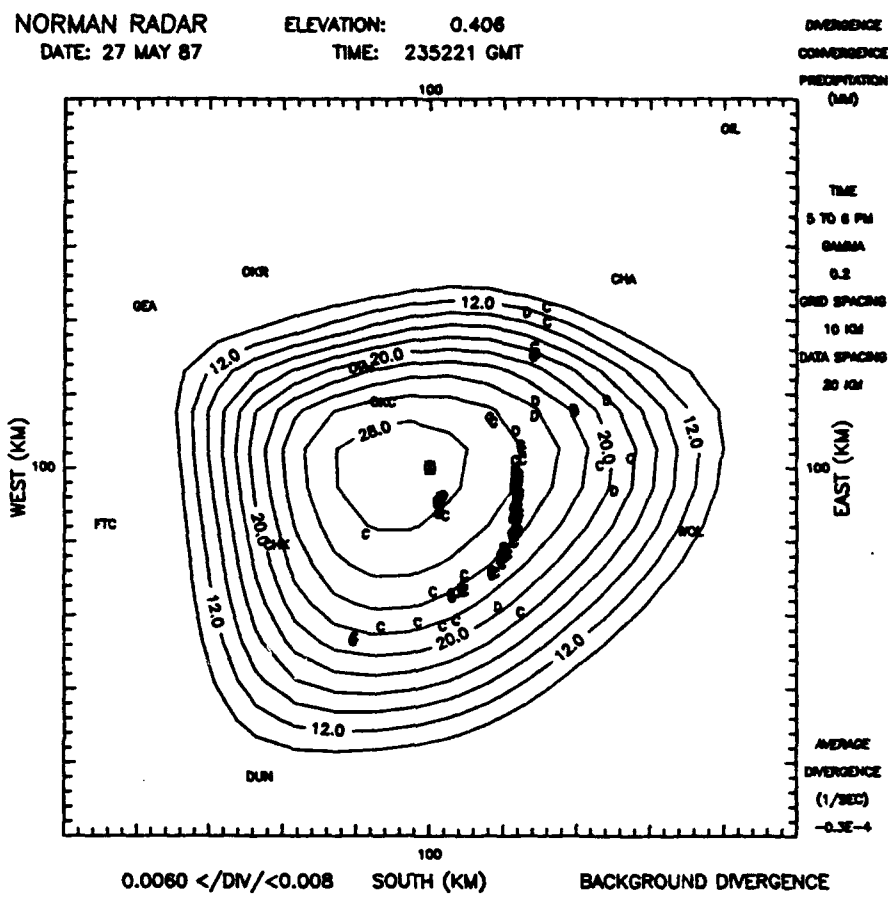


Fig. 4.14 Same as Fig. 4.2.a only for 235221 GMT (175221 CST) 27 May 1987

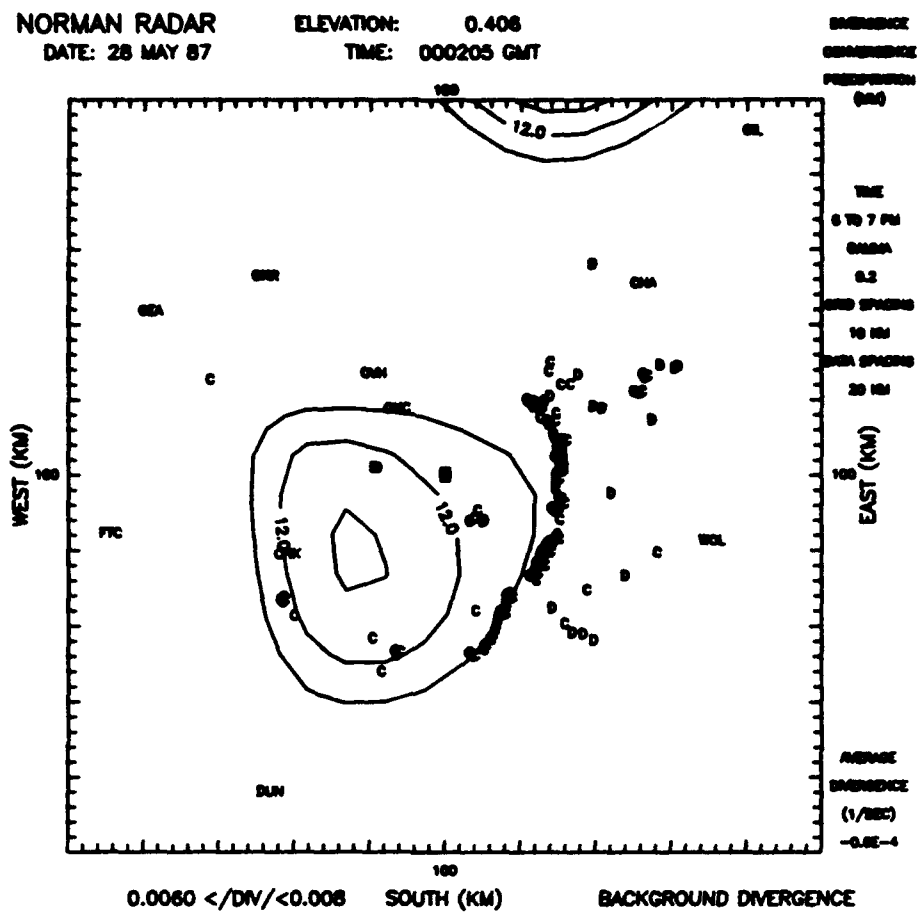


Fig. 4.15 Same as Fig. 4.2.a only for 000205 GMT (180205 CST 27 May 1987) 28 May 1987

Figures 4.13, 4.14 and 4.15 show the progression of the gust front throughout the background field. The sinusoidal nature of the average background divergence between 233256 GMT 27 May 1987 and 000205 GMT 28 May 1987 is possibly due to the rolling character of the gust front as it propagates across the surface. The average background divergence becomes positive after the gust front has reached the surface after 1810 CST (Fig. 4.16).

The average background divergence at mid-levels begins negative and becomes strongly positive by 231636 GMT (171636 CST) 27 May 1987. Recall that within this volume scan, the low-level average background divergence has reached its most negative value. Figure 4.17 shows some hints of the outflow boundary just to the south of the radar. The average background divergence remains positive through 234543 GMT (174543 CST) 27 May 1987 (Figs. 4.18, 4.19 and 4.20).

The remaining mid-level analyses show the average background divergence becoming more negative toward the end of the period (Fig. 4.21). During this time the location of the outflow boundary and its associated line of divergence singularities becomes important. Figure 4.22 shows the convergence/divergence singularity boundary stretching from Chandler to Wolf (CHA and WOL on the figure, respectively). From observational studies, we know that new convection usually occurs along the outflow

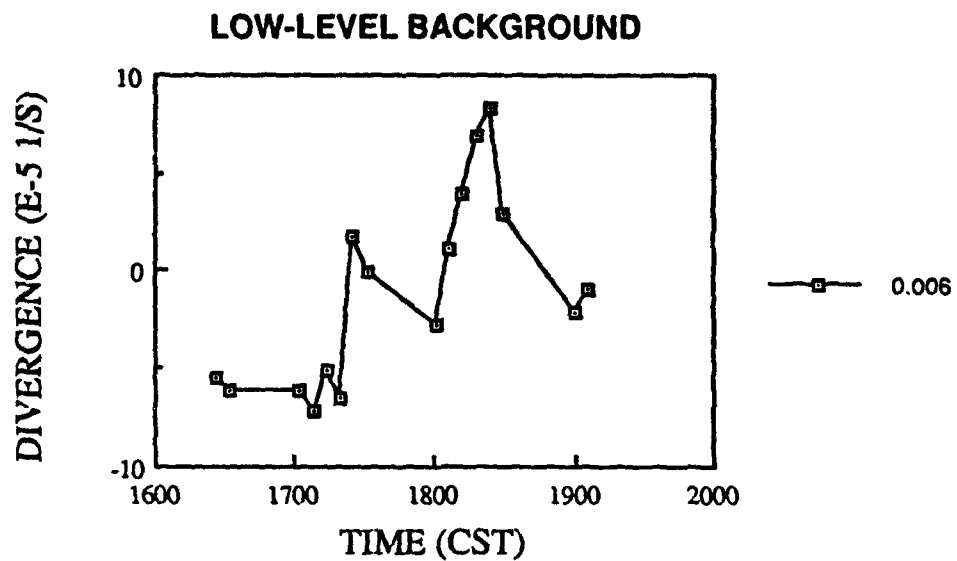


Fig. 4.16 Time-series of the low-level background divergence with the gust front contamination removed (background divergence values less than  $6 \times 10^{-3} \text{ s}^{-1}$  are averaged).

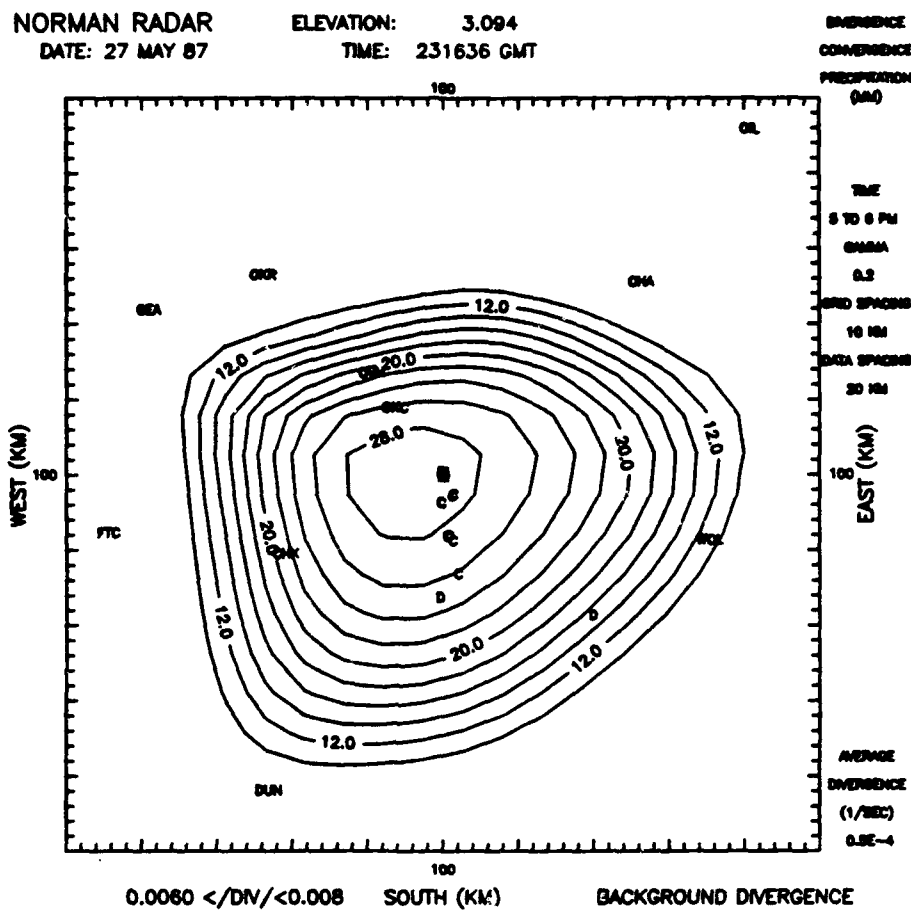


Fig. 4.17 Same as Fig. 4.2.a only for 231636 GMT (171636 CST) 27 May 1987

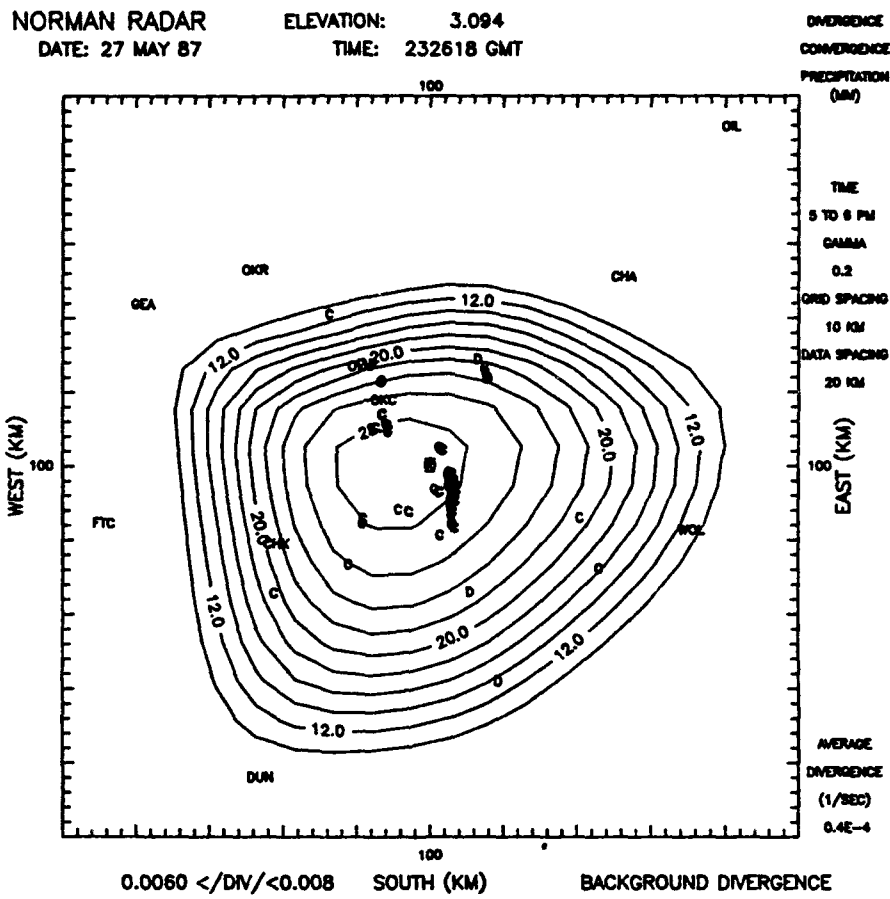


Fig. 4.18 Same as Fig. 4.2.a only for 232618 GMT (172618 CST) 27 May 1987

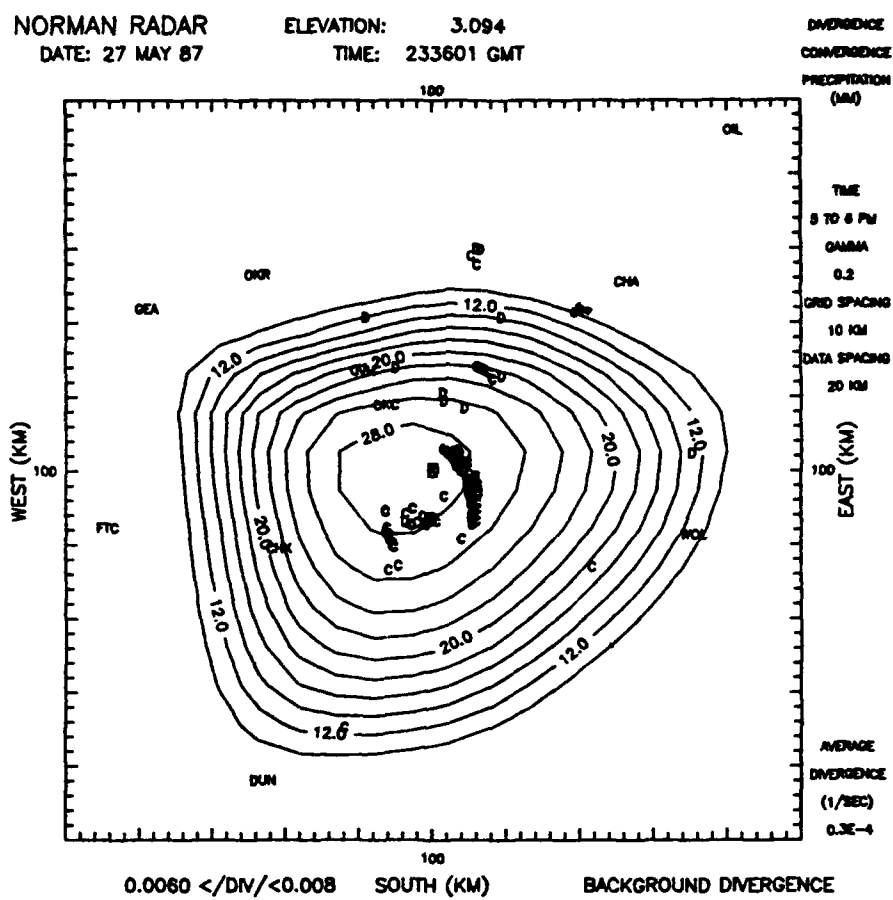


Fig. 4.19 Same as Fig. 4.2.a only for 233601 GMT (173601 CST) 27 May 1987

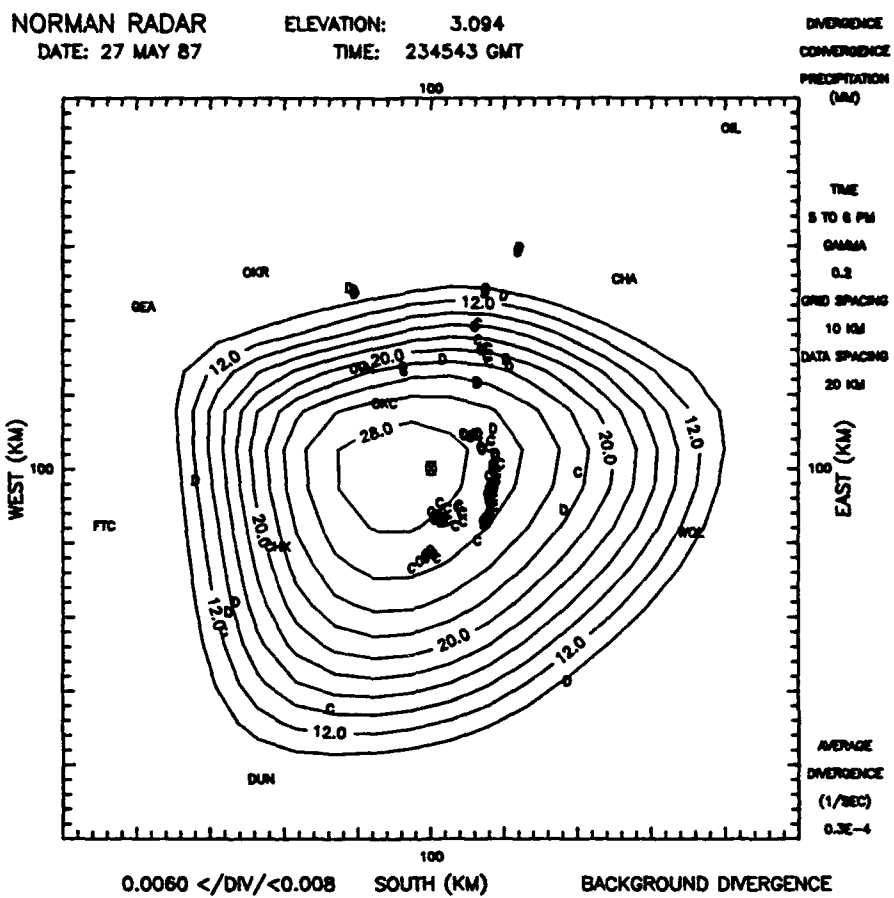


Fig. 4.20 Same as Fig. 4.2.a only for 234543 GMT (174543 CST) 27 May 1987

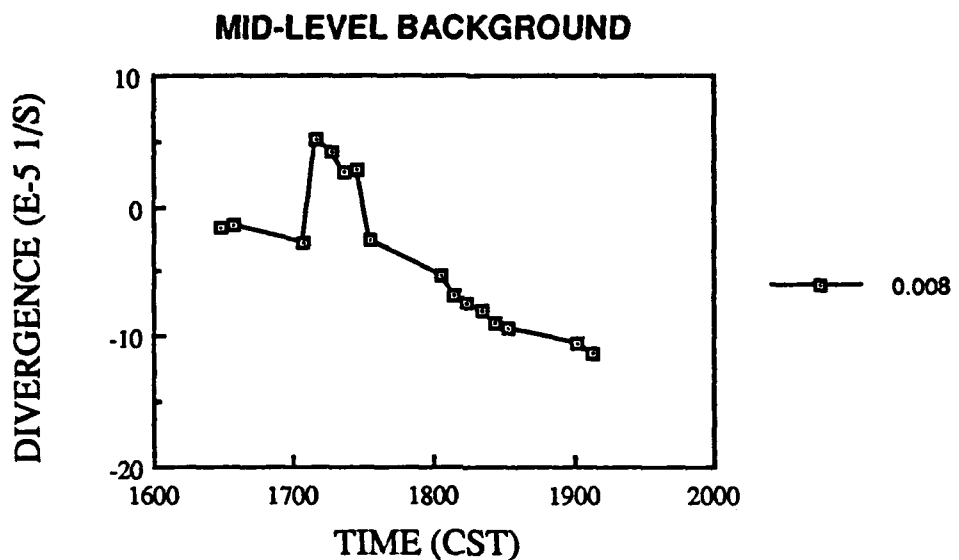


Fig. 4.21 Time-series of mid-level average background divergence including gust front contamination (divergence singularity values less than  $8 \times 10^{-3} \text{ s}^{-1}$  are averaged). Removing the gust front contamination made very little difference in this plot.

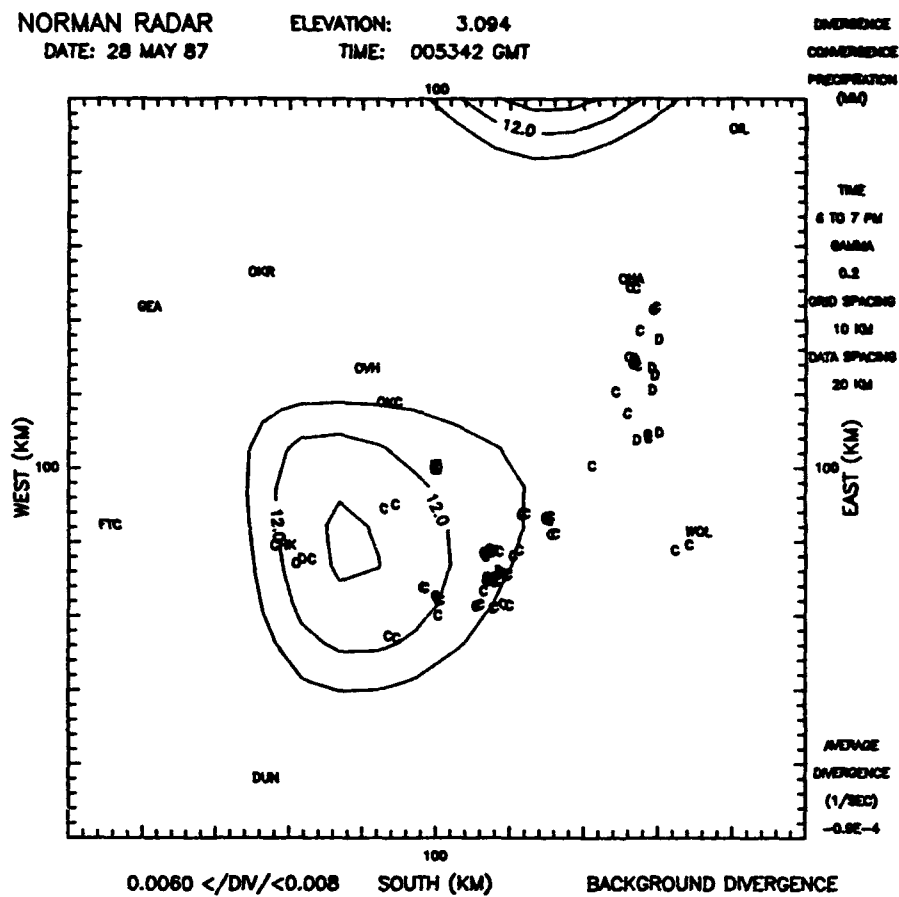


Fig. 4.22 Same as Fig. 4.2.a only for 005342 GMT (185342 CST 27 May 1987) 28 May 1987

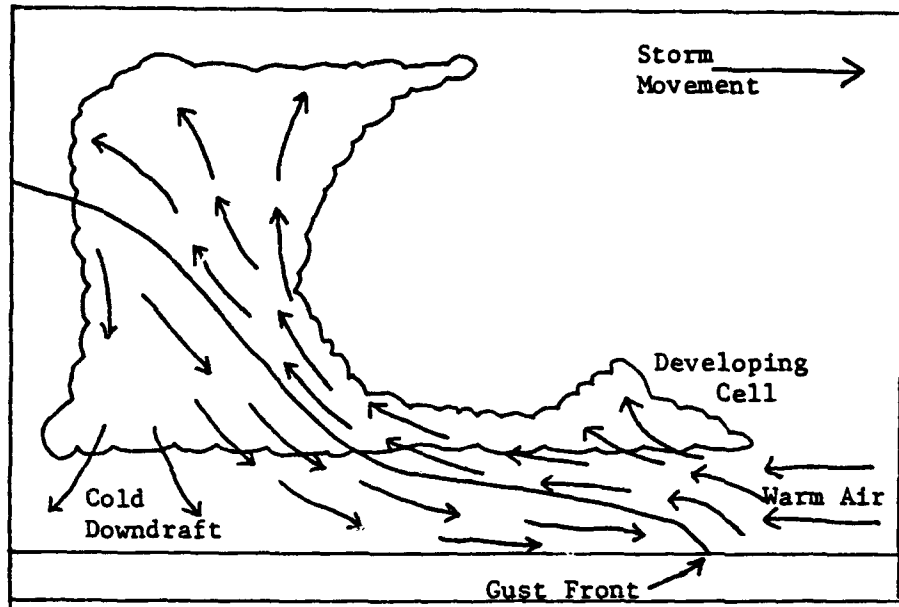


Fig. 4.23 Cross-section of a thunderstorm showing development along the gust front (After Browning, 1964; Browning and Ludlam, 1962; Browning, et al., 1976; Zipser, 1977)

boundary of a decaying thunderstorm (Fig. 4.23). The advance of the rising air just ahead of the outflow boundary is spatially correlated with the increase of rainfall during the next hour (Fig. 4.24).

At approximately the same time the average background divergence reaches a maximum at mid-levels and the low-level average divergence reaches a minimum, the rainfall reaches a maximum 50 km behind the outflow boundary indicated on the mid-level analysis. The temporal correlation between the average background divergence and the heavy precipitation were also found to be very close by Newman (1971). He found from an analysis of the NSSL surface network station observations that severe weather tends to occur at or soon after the horizontal moisture convergence at the surface reaches a maximum value. These results suggest that the low-level average background divergence and the location of the gust front can be used together for a short-term forecast of heavy precipitation by providing more accurate estimates of storm development and decay.

#### 4.3 Folded Features

Velocity folding, or aliasing, can be present at any elevation angle within a volume scan if the unambiguous velocity is low. In this particular case, aliasing was

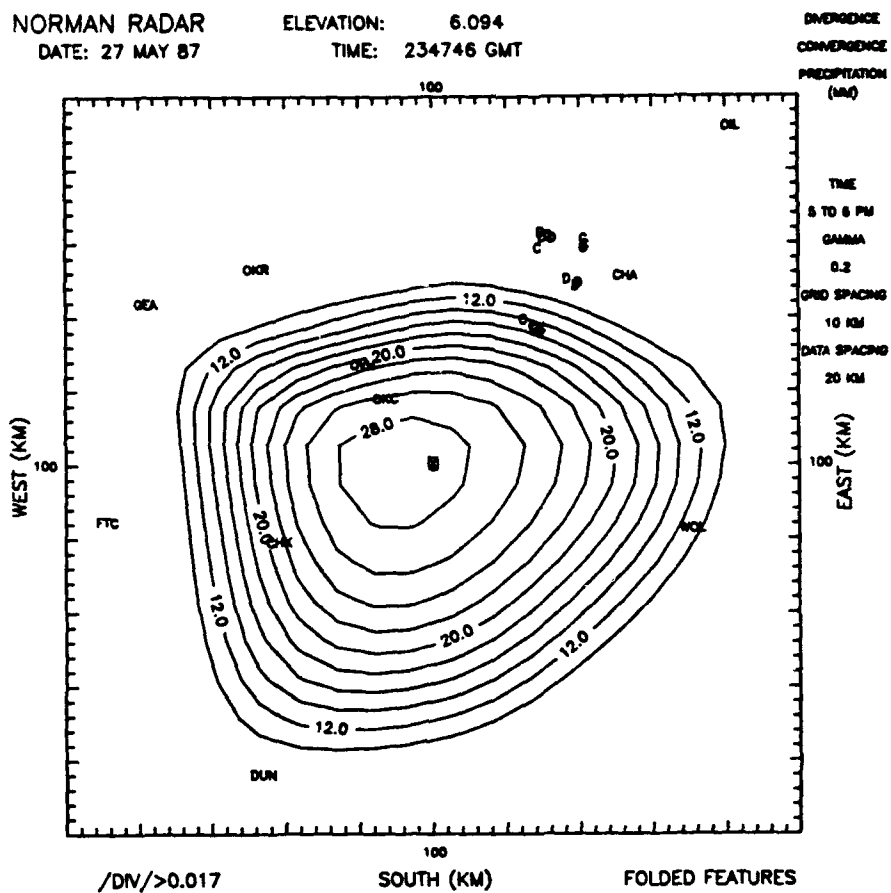


Fig. 4.24 Same as Fig. 4.2.a only for 234746 GMT (174746 CST) 27 May 1987

not a problem until the antenna elevation angle was above  $4^{\circ}$ . In particular,  $6.2^{\circ}$  is used as a representative case.

The results indicate that when the low-level average background divergence is positive, aliasing at higher elevations is present (Fig. 4.25). The low-level background divergence is most likely due to the mesohigh that forms at the surface behind the gust front.

The orientation of the convergence and divergence singularities suggest that this pattern is unique, dependent on the direction of the wind. Convergence singularities appear on the upwind side of the folded area and divergence singularities appear on the downwind side (Fig. 4.26). Based on this assumption alone, then the wind in Fig. 4.25 is blowing from southwest to northeast. The singularity analysis provides an easy way to identify aliased velocities based on the magnitude and orientation of the divergence singularities.

The dealiasing is complicated by the need to maintain continuity with the surrounding wind field. Several techniques have been developed in the last few years (Albers, 1989; Desrochers, 1989; Eilts and Smith, 1989). The most successful dealiasing algorithms are two-dimensional. Naturally, any algorithm that requires two-dimensions is not a true real-time processor. The

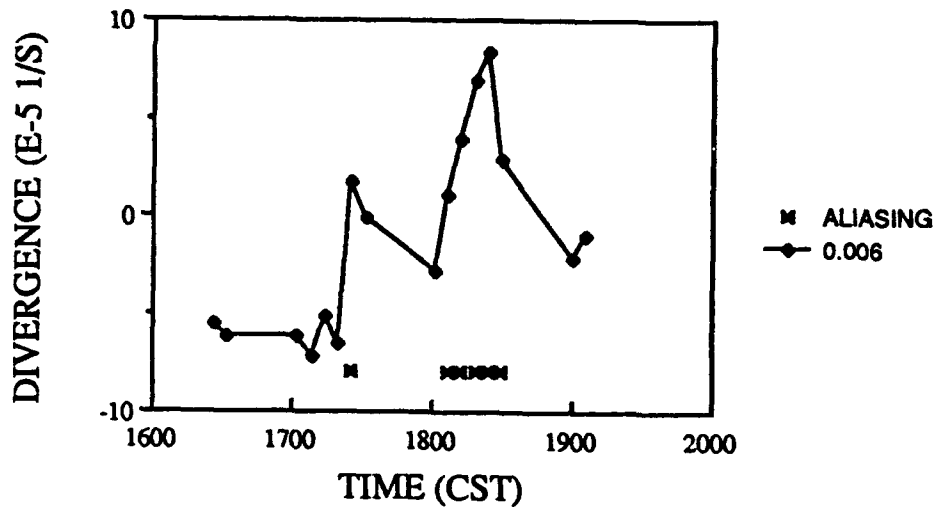
**LOW-LEVEL BACKGROUND AND UPPER-LEVEL ALIASING**

Fig. 4.25 Time-series of the low-level background divergence and the occurrence of aliasing at higher elevations. The volumes with aliasing are identified as \* along the bottom of the plot.

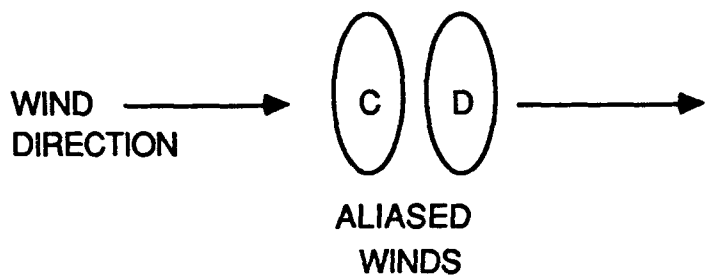


Fig. 4.26 Schematic of aliasing with respect to the singularity orientation. A region of convergence forms upwind of the aliasing and a region of divergence forms downwind of the aliasing. The singularities show the outline of the aliased area because the maximum difference in the wind velocities occur along the edges where the winds switch from positive to negative values and vice versa.

singularity analysis could (conceivably) reduce the need for dealiasing in two-dimensions, except in very rare cases. Identifying the boundaries of the region to be dealiased is easily accomplished with this technique.

We know that the measured velocity,  $V_m$ , is given by (Desrochers, 1988)

$$V_m = V_t - 2fV_n \quad (7)$$

Where:  $V_t$  = the true velocity

$V_n$  = the unambiguous velocity

$$= \frac{\lambda(\text{PRF})}{4}$$

$\lambda$  = wavelength of the radar

PRF = the pulse repetition frequency of the radar

f = the Nyquist range of the aliased velocity

The Nyquist range of the aliased velocities can be determined by using the truncated integral (Desrochers, 1988)

$$f = \text{INT} \left[ \frac{V_t}{2V_n} \right] \quad (8)$$

Once a reliable objective technique is devised to dealias the velocities, the unambiguous velocity could be reduced during convection allowing the unambiguous range to increase. We know that for a given wavelength and given unambiguous velocity, the unambiguous range is uniquely determined (Doviak and Zrnic, 1984)

$$RV_n = \frac{c\lambda}{8} = \text{constant} \quad (9)$$

Where: R = unambiguous range

c = speed of light =  $3 \times 10^8 \text{ ms}^{-1}$

So, if  $V_n$  is decreased, then R increases. Would there be any benefit from being able to increase the unambiguous range? If  $V_n$  can be reduced from  $34 \text{ ms}^{-1}$  to  $24 \text{ ms}^{-1}$  during convection, then the unambiguous range increases from 110 km to 156 km. The approximate distance between adjacent radars in the NEXRAD network will be approximately 280 km. We assume the two radars intersect at the halfway point, or 140 km, then use the lowest elevation angle, and assume the curvature of the earth can be calculated using the 4/3 earth model (Doviak and Zrnic, 1984)

$$a_e = 4/3a \quad (10)$$

Where:  $a_e$  = curvature of the earth  
 $a$  = radius of the earth

To determine the height at which the two radars intersect we plug  $r=140$  km, (10) and  $\theta_s = 0.406$  degrees into (6). We get

$$h = 2.1 \text{ km} \quad (11)$$

This means that the two radars would overlap in coverage beginning at 2.1 km in altitude and have a horizontal overlap of 32 km. The overlap would be very beneficial in maintaining observation continuity of a severe thunderstorm. Currently, the unambiguous velocity is increased to  $34 \text{ ms}^{-1}$  during convective weather in order to reduce the effects of aliasing. This also reduces the unambiguous range to 110 km, which will leave 80 km gaps in the coverage between adjacent radars in the NEXRAD network.

## **CHAPTER V**

### **CONCLUSIONS**

The amount of information a Doppler radar provides can be overwhelming. This investigation has shown that the information contained in a Doppler velocity scan can be pared down to a few hundred data points. These data points can, in turn, be broken down into three basic categories of features. The three categories are based on the order of magnitude of the divergence singularity and the orientation of the singularities.

Analysis of the storm features showed the development of a gust front can be picked up in the mid-level sweep as early as 40 minutes before the signature appears in the Doppler data in the low-level sweep. Further, the low-level sweep shows indications of the gust front 30 minutes before it is an identifiable signature. The general curvature of the gust front can also provide an estimate of where the heaviest precipitation is occurring.

The background features are the most flexible of the three categories. The low-level analysis proved to be

the best for determining where the gust front first reached the surface. It also proved very helpful in determining when there would be aliasing at high elevation angles. The average background divergence at low levels proved to be useful in determining the onset of heavy precipitation. When the low-level average background divergence reached its most negative value and the mid-level average background divergence reached its most positive value is when the heaviest precipitation occurred behind the gust front singularities. The mid-level average background divergence also was a good indicator of where the next area of heavy precipitation would occur.

Finally, the folded features showed patterns that uniquely identify the location of the aliased velocities and provided an indication of the wind direction. If the singularity analysis identification can be efficiently exploited, then the unambiguous velocity could be reduced during convective activity and the unambiguous range would be increased. By increasing the unambiguous range, it is possible to provide some overlap between adjacent radars in the proposed NEXRAD network, which would provide continuity of information about a storm as it passes through the network. Currently, the unambiguous velocity is increased during convective activity in order

to reduce the occurrence of aliasing and this practice would leave gaps in the NEXRAD network during severe weather.

The primary advantage of the singularity analysis is that it could be done in real-time and it uses a minimum of computer time. Many of the algorithms currently in use require several different sweeps to produce an analysis. This limited case study suggests that one or two sweeps separated by two or three minutes can provide almost the same information in a condensed and easily interpreted form.

## **CHAPTER VI**

### **FUTURE WORK**

There are four major areas of work that I believe would be either fascinating or instructive.

First, I would like to see the divergence singularity calculations extended to include moisture divergence. I believe the moisture divergence would be a much more indicative parameter for heavy precipitation analysis and forecasting, especially when applied at altitudes above the boundary layer.

Second, the derivation of the three-dimensional wind field from the singularity analysis would be a large task. However, I believe the winds obtained from the divergence and vorticity singularities would be very useful in nowcasting of severe weather, especially in the case of downbursts.

Third, I would like to see this technique used to help simplify the task of unfolding range folded velocities. Once the technique of unfolding has been perfected, the Nyquist frequency could be decreased and the unambiguous range increased. This would greatly

enhance the useful volume sampled by the radar and also increase the overlap between radars once the Doppler radar network is in place.

Finally, I would like to see the singularity extraction technique run side-by-side in real-time with the current NEXRAD algorithms. I believe that this technique will prove itself very useful in short-term forecasting.

## BIBLIOGRAPHY

- Albers, S. C., 1989: Two-dimensional velocity de-aliasing in highly sheared environments. Preprints, 24<sup>th</sup> Conference on Radar Meteorology, AMS, Boston, MA, 411-414.
- Atlas, D., 1964: "Advances in radar meteorology" in Advances in Geophysics. Academic Press, New York, NY, 10, 318-478.
- Auer, A. H., Jr., D. L. Veal and J. D. Marwitz, 1969: Updraft deterioration below cloud base. Preprints, 6<sup>th</sup> Conference on Severe Local Storms, AMS, Boston, MA, 16-19.
- Augustine, J. A. and K. W. Howard, 1988: Mesoscale convective complexes over the United States during 1985. *Mon. Wea. Rev.*, 116, 685-701.
- Barnes, S. L., 1964: A technique for maximizing details in numerical weather map analysis. *J. Appl. Meteor.*, 3, 396-409.
- , 1973: Mesoscale objective analysis using weighted time-series observations. NOAA Tech. Memo. ERL NSSL-62, National Severe Storms Laboratory (NSSL), Norman, OK, 60 pp.
- , 1980: Report on a meeting to establish a common Doppler radar data exchange format. *Bull. Amer. Meteor. Soc.*, 61, 1401-1404.
- Battan, L. J., 1973: Radar Observation of the Atmosphere. The University of Chicago Press, Chicago, IL, 324 pp.
- Bender, C. M., and S. A. Orszag, 1978: Advanced Mathematical Methods for Scientists and Engineers. McGraw-Hill Book Company, New York City, NY, 573 pp.

- Browning, K. A., 1964: Airflow and precipitation trajectories within severe local storms which travel to the right of the winds. *J. Atmos. Sci.*, **21**, 634-639.
- , 1982: "General circulation of middle-latitude thunderstorms" in Thunderstorms: A Social, Scientific and Technological Documentary. Vol. 2 = Thunderstorm Morphology and Dynamics. NOAA, ERL, Washington, DC, 211-247.
- , J. C. Fankhauser, J.-P. Chalon, P. J. Eccles, R. C. Strauch, F. H. Merrem, D. J. Musil, E. L. May and W. R. Sand, 1976: Structure of an evolving hailstorm. part V: synthesis and implications for hail growth and suppression. *Mon. Wea. Rev.*, **104**, 603-610.
- and F. H. Ludlam, 1962: Airflow in convective storms. *Quart. J. Royal Meteor. Soc.*, **88**, 117-135.
- and R. Wexler, 1968: The determination of kinematic properties of a wind field using Doppler radar. *J. Appl. Meteor.*, **7**, 105-113.
- Caton, P. G., 1963: The measurement of wind and convergence by Doppler radar. Preprints, 10<sup>th</sup> Weather Radar Conference, AMS, Boston, MA, 290-296.
- Clark, J. D., 1983: The GOES user's guide. NESDIS, NOAA, Washington, DC, 156 pp.
- Desrochers, P. R., 1989: A reliable method for real-time velocity unfolding. Preprints, 24<sup>th</sup> Conference on Radar Meteorology, AMS, Boston, MA, 415-418.
- Doviak, R. J., and D. S. Zrnic, 1984: Doppler Radar and Weather Observations. Academic Press, Inc., Orlando, FL, 458 pp.
- Easterbrook, C. C., 1975: Estimating horizontal wind fields by two dimensional curve fitting of single Doppler radar measurements. Preprints, 16<sup>th</sup> Radar Meteorology Conference, AMS, Boston, MA, 225-230.
- Eilts, M. D., S. H. Olsen, G. J. Stumpf, L. G. Hermes, A. Abrevaya, J. Culbert, K. W. Thomas, K. Hondl and d. Klinge-Wilson, 1991: An improved gust front detection algorithm for the TDWR. Preprints, 4<sup>th</sup> International Conference on Aviation Weather Systems, AMS, Boston, MA, J37-J42.

- , and S. D. Smith, 1989: Efficient dealiasing of Doppler velocities using local environment constraints. Preprints, 24<sup>th</sup> Conference on Radar Meteorology, AMS, Boston, MA, 194-197.
- Frashier, D. B., 1990: Lightning ground strikes analysed by singularity and fractal techniques: a mesoscale convective complex case study. Masters Thesis. The University of Oklahoma, Norman, OK, 92 pp.
- Fritsch, J. M., 1988: "Mesoscale convective complexes" in Colloquium on Synoptic Meteorology: Notes from an NCAR Summer Colloquium. NCAR, NSF, Boulder, CO, 436 pp.
- , R. J. Kane and C. R. Chelius, 1986: The contribution of mesoscale convective weather systems to the warm-season precipitation in the United States. *J. Clim. Appl. Meteor.*, **25**, 1333-1345.
- Fujita, T., 1955: Results of detailed synoptic studies of squall lines. *Tellus*, **7**, 405-436.
- , 1959: Precipitation and cold-air production in mesoscale thunderstorm systems. *J. Meteor.*, **16**, 454-466.
- Haltiner, G. J., and R. T. Williams, 1980: Numerical Prediction and Dynamic Meteorology. John Wiley & Sons, Inc., New York City, NY, 477 pp.
- Holton, J. R., 1979: An Introduction to Dynamic Meteorology. Academic Press, New York City, NY, 391 pp.
- Kessinger, C. M., 1991: Personal communication.
- Knupp, K. R., and W. R. Cotton, 1987: Internal structure of a small mesoscale convective system. *Mon. Wea. Rev.*, **115**, 629-645.
- Koch, S. E., M. DesJardins and P. J. Kocin, 1983: An interactive Barnes objective map analysis scheme for use with satellite and conventional data. *J. Clim. Appl. Meteor.*, **22**, 1487-1503.
- Lamb, H., 1932: Hydrodynamics. Cambridge University Press.
- Larson, L. W., and E. L. Peck, 1974: Accuracy of precipitation measurements for hydrologic modeling. *Water Resour. Res.*, **10**, 857-863.

- Leary, C. A., and E. N. Rappaport, 1987: The life cycle and internal structure of a mesoscale convective complex. *Mon. Wea. Rev.*, **115**, 1503-1527.
- Lhermitte, R. M., and D. Atlas, 1961: Precipitation motion by pulse Doppler radar. *Preprints, 9<sup>th</sup> Weather Radar Conference*, AMS, Boston, MA, 218-223.
- Maddox, R. A., 1980: Mesoscale convective complexes. *Bull. Amer. Meteor. Soc.*, **61**, 1374-1387.
- , 1983: Large-scale meteorological conditions associated with midlatitude, mesoscale convective complexes. *Mon. Wea. Rev.*, **111**, 1475-1493.
- , D. M. Rodgers and K. W. Howard, 1982: Mesoscale convective complexes over the United States during 1981-annual summary. *Mon. Wea. Rev.*, **110**, 1501-1514.
- Milne-Thomson, L. M., 1960: Theoretical Hydrodynamics. The Macmillan Co., New York, NY, 660 pp.
- Moncrieff, M. W., and M. J. Miller, 1976: The dynamics and simulation of tropical cumulonimbus and squall lines. *Quart. J. Royal Meteor. Soc.*, **102**, 373-39 .
- Newman, W. R., 1971: The relationship between horizontal moisture convergence and severe storm occurrences. Masters Thesis. The University of Oklahoma, Norman, OK, 51 pp.
- NOAA, 1987a: Hourly precipitation data, Vol. 33, No. 5. NCDC, NESDIS, NOAA, Asheville, NC.
- , 1987b: Storm data, Vol. 29, No. 5. NCDC, NESDIS, NOAA, Asheville, NC.
- Orlanski, I., 1975: A rational subdivision of scales for atmospheric processes. *Bull. Amer. Meteor. Soc.*, **56**, 527-530.
- Peace, R. L., Jr., R. A. Brown and H. G. Camnitz, 1969: Horizontal motion field observations with a single pulse Doppler radar. *J. Atmos. Sci.*, **26**, 1096-1103.
- Peterson, D. P., and D. Middleton, 1963: On representative observations. *Tellus*, **15**, 387-405.
- Rodgers, D. M., K. W. Howard and E. C. Johnston, 1983: Mesoscale convective complexes over the United States during 1982. *Mon. Wea. Rev.*, **111**, 2363-2369.

- , M. J. Magnano and J. H. Arns, 1985: Mesoscale convective complexes over the United States during 1983. *Mon. Wea. Rev.*, **113**, 888-901.
- Rouse, H., 1961: Fluid Mechanics for Hydraulic Engineers. Dover Publications, Inc., New York City, NY, 422 pp.
- Sasaki, Y. K., 1955: A fundamental study of the numerical prediction based on the variational principle. *J. Meteor. Soc. Japan*, **33**, 262-275.
- , 1990: Personal communication.
- , and T. L. Baxter, 1982: "The gust front" in Thunderstorms: A Social, Scientific and Technological Documentary. Vol. 2 - Thunderstorm Morphology and Dynamics, 281-296.
- , K. Mizuno, S. Allen, V. Whitehead and K. E. Wilk, 1989: Optimized variational analysis scheme of single Doppler radar wind data. Preprints, 3<sup>rd</sup> International Conference on the Aviation Weather System, AMS, Boston, MA.
- Schaefer, J. T., L. R. Hoxit, and C. F. Chappell, 1982: "Thunderstorms and their mesoscale environment" in Thunderstorms: A Social, Scientific, and Technological Documentary. Vol. 2 - Thunderstorm Morphology and Dynamics, 173-209.
- Scorer, R. S., 1978: Environmental Aerodynamics. Halsted Press, New York City, NY, 488 pp.
- Streeter, V. L., and E. B. Wylie, 1985: Fluid Mechanics. McGraw-Hill, Inc., New York City, NY, 586 pp.
- Waldteufel, P., and H. Corbin, 1979: On the analysis of single-Doppler radar data. *J. Appl. Meteo.*, **18**, 532-542.
- Witt, A., S. D. Smith, M. D. Eilts, L. G. Hermes and D. L. Klinge-Wilson, 1989: Gust front/wind shift algorithm for the Terminal Doppler Weather Radar. FAA Report No. DOT/FAA/NR-91/4, DOT, FAA, Washington, D. C.
- Wood, V. T., and R. A. Brown, 1983: Single Doppler velocity signatures: an atlas of patterns in clear air/widespread precipitation and convective storms. NOAA Tech. Memo. ERL NSSL-95, NSSL, NOAA, ERL, Norman, OK.

Zipser, E. J., 1977: Mesoscale and convective-scale  
downdrafts as distinct components of squall line  
structure. *Mon. Wea. Rev.*, 105, 1568-1589.

## APPENDIX A

The rotation of a fluid element can be represented by a vector with a length proportional to the magnitude of the rotation (radians per second) and a direction parallel to the instantaneous axis of rotation. The curl of the velocity vector is twice the rotation vector (Holton, 1979; Streeter and Wylie, 1985)

$$\nabla \times \vec{V} = 2\bar{\omega} \quad (A.1)$$

The rotation of an element about an axis is defined as the average angular velocity of two infinitesimal line segments through a point, which is mutually perpendicular to themselves and the axis

$$\omega_x = \frac{1}{2} \left[ \frac{\partial w}{\partial y} - \frac{\partial v}{\partial z} \right] \quad (A.2)$$

$$\omega_y = \frac{1}{2} \left[ \frac{\partial u}{\partial z} - \frac{\partial w}{\partial x} \right] \quad (A.3)$$

$$\omega_z = \frac{1}{2} \left[ \frac{\partial v}{\partial x} - \frac{\partial u}{\partial y} \right] \quad (A.4)$$

Irrotational flow can be defined as a flow where there is an absence of rotation at all points except singular points, so the following must be satisfied (Rouse, 1961):

$$\frac{\partial v}{\partial x} = \frac{\partial u}{\partial y} \quad (A.5)$$

$$\frac{\partial u}{\partial y} = \frac{\partial v}{\partial z} \quad (A.6)$$

$$\frac{\partial u}{\partial z} = \frac{\partial w}{\partial x} \quad (A.7)$$

Now, consider as a free body a small element of fluid shaped like a sphere. Assuming the fluid is frictionless, no tangential stresses or forces are applied to its surface. The pressure forces act normal to its surface and center. Any body forces applied to the sphere must act through its center of mass. So, no torque may be applied about any diameter of the sphere. The angular acceleration of the sphere must always be zero. If the sphere is initially at rest, then it cannot be set in

rotation. If the sphere is initially rotating, then the rotation cannot be changed. This applies at every point in the fluid and one can visualize the fluid elements as being pushed around by boundary movements, but not being rotated if initially at rest (Lamb, 1932; Rouse, 1961).

The velocity potential is a scalar function of space so that its rate of change with respect to any direction is the velocity component in that direction (Scorer, 1978):

$$\vec{V} = \nabla \phi \quad (A.8)$$

$$u = \frac{\partial \phi}{\partial x} \quad (A.9)$$

$$v = \frac{\partial \phi}{\partial y} \quad (A.10)$$

$$w = \frac{\partial \phi}{\partial z} \quad (A.11)$$

A two-dimensional flow vector  $(\phi, v)^T$  can be expressed in terms of velocity potential,  $\phi$ , and the stream function,  $v$ , given that  $x$  and  $y$  are within the domain,  $\Omega$  (Sasaki, 1990). By definition, this vector satisfies the Poisson equation:

$$\nabla^2 \begin{pmatrix} \phi \\ \psi \end{pmatrix} = \begin{pmatrix} D \\ \zeta \end{pmatrix} \quad (A.12)$$

Where:  $\nabla^2$  = 2-D Laplacian operator

D = divergence

$\zeta$  = relative vorticity

Using Green's function (Haltiner and Williams, 1980), we can solve (A.12) for  $(\phi, \psi)'$ :

$$\begin{pmatrix} \phi \\ \psi \end{pmatrix} = \iint_{\Omega} (G_s + G_h) \begin{pmatrix} D \\ \zeta \end{pmatrix} dx dy \quad (A.13)$$

The symmetric,  $G_s$ , and nonsymmetric,  $G_h$ , parts of Green's function satisfy

$$\nabla_p^2 G_s = \delta(P, Q) \quad (A.14)$$

$$\nabla_p^2 G_h = 0 \quad (A.15)$$

Here, P and Q are two points in the domain,  $\Omega$ , and  $\delta$  is the Dirac function. The Dirac function can be characterized as a mathematical idealization of a unit impulse (Bender and Orszag, 1978) at a singular point, P, where  $P=Q$ . A singular point is the point where a variable, P

in this case, approaches infinity (Boyce and DiPrima, 1977).

Solving (A.14) for  $G_s(P,Q)$ , we obtain the explicit expression:

$$G_s(P,Q) = -\left(\frac{1}{2\pi}\right) \ln\left(\frac{1}{\rho_{PQ}}\right) \quad (A.16)$$

Where:  $\rho_{PQ}$  = distance of Q from P

This shows  $G_s(P,Q)$  to be symmetric with respect to the singular point P. Using (A.16) and (A.14) to solve for the velocity components, u and v, we find

$$\nabla \begin{pmatrix} \phi \\ v \end{pmatrix} \sim \rho_{PQ}^{-1} \quad (A.17)$$

Where:  $u = \frac{\partial \phi}{\partial x} - \frac{\partial v}{\partial y}$

(A.18)

$$v = \frac{\partial \phi}{\partial y} + \frac{\partial v}{\partial x}$$

A physical example of Green's function is found in physics. For example, Green's function describes the

intensity of an electric field at P induced by a unit charge at Q. If Q is located within  $\Omega$ , the influence is expressed as  $G_s$  and if Q is on the boundary or outside of  $\Omega$ , it is expressed as  $G_h$ . So, if the sources are concentrated near the center of the domain, the symmetric part,  $G_s$ , dominates and the nonsymmetric part,  $G_h$ , is neglected. Hence,  $G_s$  represents the smaller scale flow and  $G_h$  represents the larger scale flow.

The variational formulation of (A.16) is (Sasaki, 1990):

$$J = \sum_i |v_{r_i} - \bar{v}_{r_i}| \quad (A.19)$$

Where  $\bar{v}_{r_i}$  is the observed radial velocity and  $v_{r_i}$  is the calculated velocity at a point, P, expressed as:

$$v_{r_i} = \sum_l \left( \frac{A_l}{\rho_{ll}} \cos \theta_{lj} - \frac{B_l}{\rho_{ll}} \sin \theta_{lj} \right) \quad (A.20)$$

$A_l$  and  $B_l$  in (A.20) determine the strength of the rotational and divergent parts of the singularity, respectively. They can be determined using the system of Euler-Lagrange equations suggested by (A.19):

$$\sum_k \left\{ \left( \sum_l \frac{\cos \theta_{lj} \cos \theta_{kj}}{\rho_{ll} \rho_{kk}} \right) A_k - \left( \sum_l \frac{\cos \theta_{lj} \sin \theta_{kj}}{\rho_{ll} \rho_{kk}} \right) B_k \right\} = \sum_l \frac{\cos \theta_{lj}}{\rho_{ll}} \bar{v}_{r_l} \quad (A.21)$$

$$\sum_k \left\{ \left( \sum_j \frac{\sin \theta_{ij} \cos \theta_{kj}}{\rho_{ij} \rho_{kj}} \right) A_k - \left( \sum_j \frac{\sin \theta_{ij} \cos \theta_{kj}}{\rho_{ij} \rho_{kj}} \right) B_k \right\} = \sum_j \frac{\sin \theta_{ij}}{\rho_{ij}} \delta_{rj} \quad (A.22)$$

We want to minimize (A.19) so as to optimize the wind components calculated. Using  $\delta_{rj}$ , the singularity strength is calculated. Local symmetry then allows us to assume a two-dimensional value of the singularity strength from the one-dimensional  $\delta_r$  value. Thus, we can assume a value for D and  $\zeta$  which is twice the singularity strength. We can then substitute into (A.13) and solve for u and v using (A.18). These horizontal velocities are then used to calculate  $\delta_{rj}$  and substitute into (A.19). The process is iterated until J reaches a minimum or falls within a prescribed error limit.

We have assumed a two dimensional simple source with a constant source strength and irrotational flow ( $\zeta=0$ ). We can express the local velocity potential about a singular point  $(\xi, \eta)$

$$\phi(x, y) = \int \int [G_s(r) + G_h] D(\xi, \eta) d\xi d\eta \quad (A.23)$$

Where:  $(x, y)$  = a point local to the singular point

$$r = [(x - \xi)^2 + (y - \eta)^2]^{1/2}$$

Locally, the symmetric Green's function predominates. The homogeneous Green's function represents the large scale (environmental) flow and is ignored:

$$\phi(x, y) = \iint G_s(r) D(\xi, \eta) d\xi d\eta \quad (A.24)$$

The symmetric Green's function is given by:

$$G_s(r) = \frac{1}{2\pi} \ln r \quad (A.25)$$

From fluid mechanics, the radial velocity of a simple source can be expressed as (Streeter and Wylie, 1985)

$$V_r = \frac{\partial \phi}{\partial r} \quad (A.26)$$

Operating on (A.24) and substituting  $d\xi d\eta = r dr d\theta$

$$\begin{aligned} V_r &= \frac{\partial \phi}{\partial r} = \iint \frac{\partial}{\partial r} \left[ \frac{1}{2\pi} \ln r D(\xi, \eta) d\xi d\eta \right] \\ &= \iint \frac{\partial}{\partial r} \left[ \frac{1}{2\pi} \ln r D(\xi, \eta) r dr d\theta \right] \end{aligned} \quad (A.27)$$

Integrating, we get

$$V_r = D(\xi, \eta)r + \frac{D(\xi, \eta)}{r} \quad (A.28)$$

Combining the two parts of the solution, we obtain the Rankine combined velocity profile. The inner, linear portion of the profile is represented by the first term on the right hand side of (A.28). The outer, decaying portion of the profile is represented by the second term on the right hand side of (A.27).

## APPENDIX B

Using Koch, et al. (1983), as a guide, the analysis parameters for the precipitation analysis are derived. We begin by determining the random data distribution:

$$\Delta n_r = A^{1/2} \left[ \frac{1 + M^{1/2}}{M - 1} \right] \quad (B.1)$$

Where:  $\Delta n_r$  = random data distribution = 77.668 km

$A$  = area of the raingage network = 116,000 km<sup>2</sup>

$M$  = number of raingage observations = 29

The random data distribution is the average distance between stations within a square area,  $A$ , if  $M$  stations are uniformly distributed across the area. According to Koch, et al. (1983), the random data distribution is a simple guide for establishing the upper limit of the data spacing to be used in the analysis. We use the computed data spacing (the average distance between each observation and its nearest neighbor) as the lower limit, so that

$$\Delta n_1 \leq \Delta n \leq \Delta n_2$$

(B.2)

$$40.269 \text{ km} \leq \Delta n \leq 77.668 \text{ km}$$

The Gaussian nature of the filter (low-pass) allows the greatest increase in response at shorter wavelengths when the final response of the analysis at the smallest resolvable horizontal wavelength ( $\lambda$ ) is constrained by

$$\lambda = 2\Delta n < e^{-1} : type = text$$

$$2\Delta n = \pi \left[ \frac{-K_o}{\ln D_o(2\Delta n)} \right]^{1/2} \quad (B.3)$$

$$\text{where: } -K_o = \left( \frac{\lambda}{\pi} \right) \ln D_o(\lambda) = \text{constant} \quad (B.4)$$

Substituting (B.4) into (B.3):

$$2\Delta n = \lambda \left[ \frac{\ln D_o(\lambda)}{\ln D_o(2\Delta n)} \right]^{1/2} \quad (B.5)$$

Which yields

$$\left[ \frac{\lambda}{2\Delta n} \right]^2 = \frac{\ln D_o(2\Delta n)}{\ln D_o(\lambda)} \quad (B.6)$$

Solving for  $D_o(\lambda)$ :

$$D_o(\lambda) = D_o(2\Delta n)^t \quad (B.7)$$

Where:  $\xi = \left( \frac{2\Delta n}{\lambda} \right)^2$

So, if  $\lambda = 2\Delta n$ , then  $D_o(\lambda) = D_o(2\Delta n) = e^{-1} = 0.37$ .

We now know

$$D_o(\lambda) = D_o(2\Delta n) = \exp \left[ -K_o \left( \frac{\pi}{2\Delta n} \right)^2 \right] \quad (B.8)$$

Solving for the filter shape function,  $K_o$ , for the first pass

$$K_o = - \left( \frac{2\Delta n}{\pi} \right)^2 \ln [D_o(2\Delta n)] \quad (B.9)$$

The question now becomes: What is the value of  $D_o(2\Delta n)$ ? We require the response function after the first pass to be (after Barnes, 1973):

$$D_1 = \exp \left[ -K_1 \left( \frac{\pi}{\lambda} \right)^2 \right] \quad (B.10)$$

Where:  $K_1$  = the filter shape function for the second pass  
 $= \gamma K_o$

Gamma, the numerical convergence parameter, forces the convergence between the observed field and the second (correction) pass interpolated field. Substituting for  $K_1$  in (B.10)

$$D_1 = \exp \left[ -\gamma K_o \left( \frac{\pi}{\lambda} \right)^2 \right] \quad (B.11)$$

According to Koch, et al. (1983), the interactive Barnes scheme provides the most detail when gamma is close to 0.2 and the least when gamma is close to 1.0:

$$0.2 \leq \gamma \leq 1.0 \quad (B.12)$$

If the value of gamma is less than 1.0, the weighting factor is decreased between passes one and two, producing better agreement with the observations. What we are looking for is a balance between approaching the original amplitude and minimizing the final response of the small wavelengths. We want the small wavelengths to remain

below a pre-determined amplitude in order to reduce the noise. In choosing a value of gamma, we consider the following:

1. How closely do we want the analysis to fit the data?
2. Eliminate contamination by sub-grid scale atmospheric processes (not necessarily a major problem in our case).
3. The degree of spacial uniformity of the data (areal coverage was chosen to maximize the uniformity of the data coverage).

For this particular analysis, we chose  $\gamma = 0.2$ .

Barnes (1964) determined the spectral response after one pass through the data (assuming the data can be represented by two-dimensional Fourier integrals):

$$D_o = \exp \left[ -K_o \left( \frac{\pi}{\lambda} \right)^2 \right] \quad (B.13)$$

Substituting (B.13) into (B.11), we obtain

$$D_1 = D_o^\gamma \quad (B.14)$$

Koch, et al. (1983), determined the response function,

$D_N^*$ , after the  $N^{th}$  iterative pass to be

$$D_N^* = D_o + (1 - D_o)(D_1 + \psi_N); \quad 2 \leq N \leq \infty \quad (B.15)$$

Where:  $D_1 = D_o^\gamma$

$$\psi_N = \sum_{i=2}^N \left[ D_i \prod_{j=2}^i (1 - D_{j-1}) \right]$$

Since we desire convergence of the field and the difference between the observed and interpolated fields is constant (Koch, et al., 1983):

$$\begin{aligned} \psi_N &= 1 - D_1 \\ &= 1 - D_o^\gamma \end{aligned} \quad (B.16)$$

We further require

$$D_1(2\Delta n) = e^{-1} = 0.37 \quad (B.17)$$

Substituting (B.17), (B.16),  $j = 2$  and  $N = 2$  into (B.15):

$$\begin{aligned} D_1(2\Delta n) &= D_o + (1 - D_o)(D_1 + 1 - D_1) \\ &= D_o(1 + D_o^{\gamma-1} - D_o^\gamma) = 0.37 \end{aligned} \quad (B.18)$$

Substituting for gamma and solving for  $D_o$  ( $\gamma = 0.2$ ):

$$D_o(2\Delta n) = 0.0064$$

(B.19)

So, if  $\lambda = 2\Delta n$ , then  $D_o(\lambda) = D_o(2\Delta n)$ .

Using (B.9) and (B.2), we now have

$$K_o = 12,349.836 \text{ km}^2$$

(B.20)

Now that we've determined the maximum value of  $K_o$ , we turn our attention to objectively determining the grid spacing. We require a minimum of five grid points to resolve a wave (Peterson and Middleton, 1963) on a grid. If the minimum resolvable wave is  $\lambda$ , then our grid spacing must be no larger than one half of the data spacing (Fig. A.2.1). Restricting the value of the grid spacing in this way helps to keep derivatives on the grid

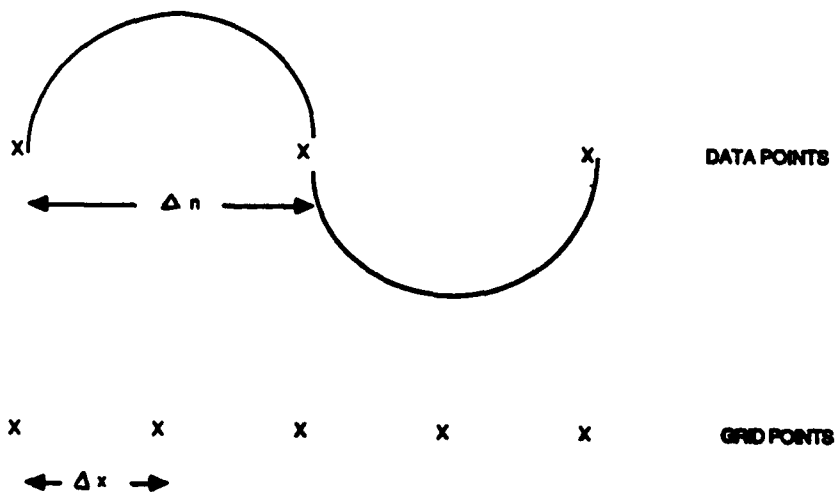


Fig. B.1 The relationship between the grid size and data spacing (After Peterson and Middleton, 1963; Koch, et al., 1983)

from becoming too noisy and allows one to represent only resolvable features (Koch, et al., 1983). The GEMPAK program uses a Barnes scheme with (Koch, et al., 1983):

$$\frac{1}{3} \leq \frac{\Delta x}{\Delta n} \leq \frac{1}{2} \quad (B.21)$$

Using (B.2), we find the upper limits on the grid spacing are

$$25.889 \text{ km} \leq \Delta x \leq 38.834 \text{ km} \quad (B.22)$$

and the lower limits on the grid spacing are

$$13.423 \text{ km} \leq \Delta x \leq 20.135 \text{ km} \quad (B.23)$$

We also want to reduce the effects of "ballooning" in our analysis (errors are introduced along the edge of data sparse regions) which are due to an insufficient number of data points determining the value of a given grid point (Koch, et al., 1983). These effects can be reduced in three ways:

1. Require three or more data points to determine the value at a grid point.

2. Choose the analysis domain so there are several observations outside the analysis grid.

3. Use a sufficiently large cut-off radius,  $R_c$ , to allow each grid point enough observation influence to be representative of the field at that point.

The cut-off radius allows us to reduce the amount of computer time used by eliminating the calculation of extremely small weights (Koch, et al., 1983) without affecting the overall quality of the analysis. How do we choose the optimal value of the cut-off radius? Koch, et al. (1983), recommended the following

$$R_c = (20K_s)^{1/2} \quad (B.24)$$

For our case,  $R_c = 496.988$  km, which when squared is roughly twice the area of our data domain. Using this value of  $R_c$  in our analysis will guarantee a minimum of three observations for each grid point, so the filter response characteristics should remain unaffected. Koch, et al. (1983), then recommend using an influence radius,  $R$ , in the calculations such that

$$\frac{R_c}{R} = 4.5 \quad (B.25)$$

Using the value of  $R_c$  determined with (B.24) we obtain  $R = 110.442$  km. Another check on the value of the cut-off radius is (Koch, et al., 1983):

$$\frac{R_c}{\Delta x} = 12.8 \quad (B.26)$$

provided we assume  $\Delta n = 2\Delta x$ .

In this analysis, we have maintained the objectivity by (Koch, et al., 1983)

1. limiting the value of gamma internally, keeping the number of passes through the data to two and constraining

$$\Delta x \left( \frac{\Delta n}{3} \leq \Delta x \leq \frac{\Delta n}{2} \right) \text{ and } \Delta n \left( \Delta n \geq \Delta n_c \right).$$

2. allowing the weights to be determined solely by the data spacing and internally calculating the weights so as to filter the  $2\Delta n$  wave entirely.